DISCRETE AND CONTINUOUS
DYNAMICAL SYSTEMS SERIES S

doi:10.3934/dcdss.2022036

WIGGLY CANARDS: GROWTH OF TRAVELING WAVE TRAINS THROUGH A FAMILY OF FAST-SUBSYSTEM FOCI

Paul Carter*

Department of Mathematics
University of California, Irvine
Irvine, CA 92697, USA

Alan R. Champneys

Department of Engineering Mathematics
University of Bristol
Bristol BS8 1UB, UK

Abstract. A class of two-fast, one-slow multiple timescale dynamical systems is considered that contains the system of ordinary differential equations obtained from seeking travelling-wave solutions to the FitzHugh-Nagumo equations in one space dimension. The question addressed is the mechanism by which a small-amplitude periodic orbit, created in a Hopf bifurcation, undergoes rapid amplitude growth in a small parameter interval, akin to a *canard explosion*. The presence of a saddle-focus structure around the slow manifold implies that a single periodic orbit undergoes a sequence of folds as the amplitude grows. An analysis is performed under some general hypotheses using a combination ideas from the theory of canard explosion and Shilnikov analysis. An asymptotic formula is obtained for the dependence of the parameter location of the folds on the singular parameter and parameters that control the saddle focus eigenvalues. The analysis is shown to agree with numerical results both for a synthetic normal-form example and the FitzHugh-Nagumo system.

1. **Introduction.**

Singularly perturbed systems of reaction-diffusion partial differential equations (PDEs) have shown remarkable success in modelling a wide variety of biological wave propagation phenomena, including neuronal pulses, cardiac tissue activation and calcium cell signalling. See, for example [23, 13]. Many of these problems naturally lead, when posed in a traveling wave frame, to systems of slow-fast ordinary differential equations (ODEs). One of the most studied canonical models of this class is that introduced by FitzHugh and Nagumo [14, 30] as a simplification of the Hodgkin-Huxley model of nerve signal propagation along the axon of the giant squid.

Individual pulse-solutions of the PDE typically represent homoclinic solution of the travelling wave ODEs. The bifurcation structure of homoclinic orbits in the 3-dimensional travelling wave FitzHugh-Nagumo ODE system has been studied by a number of authors both numerically [8, 18, 17, 28] and analytically [4, 5, 19, 20, 21,

---

2020 *Mathematics Subject Classification.* Primary: 34E17; Secondary: 34C23, 37G15, 35C07.

Key words and phrases. Canards, traveling waves, periodic orbits, FitzHugh–Nagumo system, geometric singular perturbation theory.

The first author is supported by NSF grant DMS-2016216.

* Corresponding author: Paul Carter.

24]. Within appropriate parameter regions these orbits connect to an equilibrium solution that is of saddle-focus type. That is the linearization is of the form

$$\begin{aligned}\dot{x} &= -\alpha x - \omega y\\ \dot{y} &= \omega x - \alpha y\\ \dot{z} &= \beta z\end{aligned}$$

with $\alpha, \beta, \omega > 0$. Such homoclinic orbits are often said to be of Shilnikov type, following the pioneering work of L.P. Shilnikov [33]. Defining $\delta = \alpha/\beta$ then under the condition $\delta < 1$ the dynamics in the neighbourhood of the homoclinic orbit are known to be chaotic, featuring dynamics that is conjugate to shift dynamics on arbitrary many symbols (see [34] and references therein). (This condition $\delta < 1$ is typically written in the Russian literature as $\sigma > 0$, where $\sigma = \beta + \alpha$ is the so-called saddle index.)

Also, as first shown by Glendinning and Sparrow [16], in the case $\delta < 1$ the homoclinic orbit is approached by family of periodic orbits of increasing period that lie on a single wiggly curve in parameter versus period (see e.g. Fig. 10 below for a topologically equivalent figure, albeit with vertical axis having a different meaning). The asymptotic calculations in [16] (see also [15]) reveal the asymptotics of the wiggly curve. Specifically, if λ_i is the difference in parameter value of the ith fold from that of the homoclinic orbit and T_i is the period of the corresponding periodic orbit then

$$\lim_{i\to\infty}(T_{i+1} - T_i) = \pi/\omega, \qquad \lim_{i\to\infty}(\lambda_{i+1} - \lambda_i) = -\exp(\pi\alpha/\omega). \tag{1}$$

This theory then shows how a travelling pulse solution is approached by a family of periodic wave trains as period tends to infinity. In the slow-fast ODE systems, such wavetrains are represented by relaxation oscillations. Also of interest, and the main topic of this paper, is the mechanism of birth of such relaxation oscillations. We shall see that, under certain mild hypotheses, the growth in amplitude (rather than period) of such orbits follows a kind of wiggly curve that is reminiscent of the Shilnikov wiggle and obeys asymptotic scalings that are analogous to (1) in the case $\delta < 1$, under a suitable re-definition of the parameters α, β, ω and T.

This paper specifically concerns three-dimensional systems like the FitzHugh-Nagumo travelling-wave equation that are of two-fast, one-slow type, although the results are likely to apply to high-dimensional systems under appropriate centre manifold reduction, for example the various models for calcium waves considered in [8]. Such systems with parameter regions where an equilibrium is globally stable are often said to feature excitability if there is a threshold to the size of perturbation that can elicit large-amplitude transient behaviour before the trajectory settles back to quiescence. As parameters are varied, the equilibrium can undergo a Hopf bifurcation, leading to a small amplitude limit cycle. Such a limit cycle is usually short-lived though and a rapid expansion in its amplitude occurs leading to characteristic large-amplitude relaxations oscillations. Such amplitude growth typically occurs in a parameter region that is exponentially thin as a function of the singular parameter ε.

Such behavior can be understood using geometric singular perturbation theory (see [27] and references therein), in particular the existence of *canard* trajectories [1, 12]. Setting $\varepsilon = 0$ to freeze slow variables yields the *fast subsystem* (also referred to as layer problem). Similarly, the $\varepsilon = 0$ limit of the slow-time dynamics gives the *slow subsystem* (also referred to as reduced system) which applies on the *critical* *manifold* $\mathcal{C}_0$ which is both the set of equilibria of the layer problem and the phase space of the slow subsystem. The classical canard phenomenon can occur in planar systems such as the unforced van der Pol oscillator, for which the one-dimensional $\mathcal{C}_0$ has a characteristic cubic shape. The canard represents a trajectory that passes very close to the unstable part of $\mathcal{C}_0$ and leads to the birth of large-amplitude relaxation oscillations from a small amplitude limit cycle.

Subsets of $\mathcal{C}_0$ that are not normally hyperbolic provide a challenge and typically represent points at which solution trajectories can separate from the perturbed slow manifold $\mathcal{C}_\varepsilon$ for small $\varepsilon > 0$. One way to resolve such problems is to introduce an auxiliary system obtained by rescaling time so that the fold points of $\mathcal{C}_0$ become singularities of the slow flow. Folded singularities give a way to analyse canard solutions, which flow through successively through the attracting and repelling parts of $\mathcal{C}_0$, by passing close to one of these singularities, see e.g. [26, 36].

Such folded singularities in three-dimensional systems with two slow and one fast variable can lead to additional oscillations in the large amplitude limit cycles through either so-called folded nodes or folded saddle nodes. Then a folded node singularity that connects a region of oscillatory dynamics to a canard trajectory can lead to the onset of so-called mixed-mode periodic orbits [9, 38].

The mechanism to be addressed in the present study is rather different, and concerns three-dimensional systems with two fast variables and one slow. Motivated by what has been observed in the FitzHugh-Nagumo model [5], and in other systems [7, 8], we consider where the growth in amplitude of a limit cycle coincides with the addition of additional folds around the slow manifold. In so doing, we find wiggly curves in amplitude of limit cycles against parameter.

The rest of this paper is outlined as follows. Section 2 introduces the FitzHugh–Nagumo equation and its underlying dynamics in the parameter region of concern here. We present numerical evidence for a wiggly canard explosion. Motivated by this, in §3, we consider a general three-dimensional slow-fast system which admits the geometry necessary to produce this behavior and describe how canard orbits arise in this general system. This construction is used as the basis in §4 for a formal asymptotic analysis of the folds in the bifurcation diagram associated with the canard explosion. Then §5 presents detailed numerical evidence for the predictions of the theory on two examples: a specifically constructed "normal form" example, and the previously studied FitzHugh-Nagumo system. Finally §6 draws conclusions and suggests avenues for future work, in particular connections to bifurcation theories for complex mixed-mode wavetrains.

2. **The FitzHugh-Nagumo equations.**

The analysis in this paper is motivated by travelling-waves in the classical FitzHugh-Nagumo PDE, given by

$$\begin{aligned} v_t &= Dv_{xx} + f(v;\lambda) - w + p \\ w_t &= \varepsilon\,(v - \gamma w) \end{aligned} \tag{2}$$

where the cubic nonlinearity is given by $f(v;\lambda) = v(1-v)(v-\lambda), 0 < \lambda < 1/2$, and the parameters $0 < \varepsilon \ll 1$, $p \geq 0$ and $\gamma \geq 0$ taken so that $(v, w) \equiv 0$ is the only homogeneous equilibrium of (2). The equation (2) was originally proposed as a simplification of the Hodgkin Huxley equations describing propagation of impulses along nerve fibers; its variants have been studied in depth the past several decades. In this context, v is a voltage-like variable, while w is a combined recovery variable which acts on a slower timescale. The parameter λ represents an excitation threshold, while $p \geq 0$ is an applied current.

Of particular interest are traveling wave solutions $(v,w)(x,t) = (v,w)(x+st)$ which represent profiles with fixed shape that travel through the domain with constant speed. Such solutions satisfy the associated traveling wave ordinary differential equation

$$\begin{aligned} \dot{v} &= d \\ \dot{d} &= \frac{1}{D}\left(sd - f(v;\lambda) + w - p\right) \\ \dot{w} &= \frac{\varepsilon}{s}\left(v - \gamma w\right) \end{aligned} \tag{3}$$

where $\dot{()} = \frac{\mathrm{d}}{\mathrm{d}\xi}$, and $\xi = x + st$. The system (3) exhibits remarkably rich dynamics and has since become a prototype model in the study of slow-fast dynamical systems. System (3) is a two-fast-one-slow ODE with a one-dimensional cubic critical manifold $\mathcal{C}_0 = \{d = 0, w = f(v;\lambda) - p\}$, consisting of two normally hyperbolic saddle-type outer branches and a repelling middle branch meeting at two nonhyperbolic fold points. Traveling waves are constructed using geometric singular perturbation theory by perturbing from singular orbits composed of portions of these branches of the critical manifold concatenated with fast jumps between the branches, which are solutions of the corresponding layer problem

$$\begin{aligned} \dot{v} &= d \\ \dot{d} &= \frac{1}{D}\left(sd - f(v;\lambda) + w - p\right) \end{aligned} \tag{4}$$

for fixed values of w.

It has been shown, for instance, that (3) admits families of homoclinic orbits, amounting to traveling pulse solutions of (2). The dynamics and properties of these pulse solutions have garnered much interest and have been studied in detail. The current work is concerned with traveling wave-train solutions, or spatially periodic pulse patterns, of (2), in particular those which arise from canard dynamics. Such solutions amount to periodic orbits of the traveling wave equation (3). These periodic waves can either be constructed from orbits which traverse only normally hyperbolic portions of $\mathcal{C}_0$ [35], or can contain orbit segments which pass near one or both of the non hyperbolic fold points. Both families of orbits represent periodic pulse patterns of (2), and have been shown to organize invading pattern-forming fronts in (2) [6].

Here, we are concerned with orbits associated with canard dynamics in (3). These originate in a singular Hopf bifurcation which occurs at the origin for a suitable value of $\lambda = \lambda_H(\varepsilon)$ and grow into large-amplitude wave trains along a canard explosion; see Figures 1 and 2. This transformation resembles the classical planar canard explosion [26], though with some subtle differences arising due to the three-dimensional nature of the traveling wave equation (3). In particular, the bifurcation branch exhibits a series of folds, which are especially pronounced near the upper part of the bifurcation branch.

Remark 1. While the bifurcation branch in the classical planar canard explosion can exhibit a finite number of folds (as $\varepsilon \to 0$) which arise due to zeros in the so-called way-in-way-out function [26], we will see that the folds appearing in Figure 2 appear due to oscillatory dynamics in the fast subsystem, and the number of folds grows like $\mathcal{O}(1/\varepsilon)$ as $\varepsilon \to 0$. Similar behavior has been observed in the context of

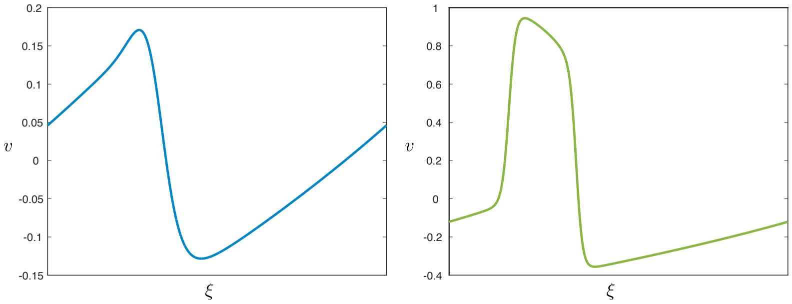

FIGURE 1. Traveling wave trains obtained in the FitzHugh–Nagumo equation (2) for $\varepsilon = 0.005, \gamma = p = 0$ with wave speed $s = 0.65$: small amplitude canard cycle (left), and a large amplitude relaxation oscillation (right), corresponding to the blue and green orbits, respectively, depicted in Figure 2.

traveling wavetrain solutions in other systems, such as the Oregonator model [32]. We further note that the phenomenon observed here is reminiscent of that which occurs along a pulse-replicating branch of traveling *pulse* solutions in the FitzHugh–Nagumo system, in which a single pulse transforms into a double pulse via a canard transition [5], along a so-called homoclinic banana. This branch exhibits a similar (and closely related) sequence of folds, growing in number as $\varepsilon \to 0$. We discuss these connections in further detail in §6.

We note that for $p = 0, s > 0$ and $\gamma \geq 0$ taken small enough, there is a single equilibrium for the full system (3) which occurs at the origin $(v, d, w) = (0, 0, 0)$. In the limit $\varepsilon \to 0$, this equilibrium lies precisely on the lower left fold point of the critical manifold $\mathcal{C}_0$ when $\lambda = 0$. For sufficiently small $\varepsilon > 0$, the canard explosion in Figure 2 originates in a Hopf bifurcation occurring at this equilibrium at a value $\lambda = \lambda_H(\varepsilon) = \mathcal{O}(\varepsilon)$.

To understand the geometry of the canard explosion in Figure 2, we consider the slow/fast geometry of (3). Setting $\varepsilon = 0$ in (3), we obtain the layer problem (4), in which w acts as a parameter. The set of equilibria of this system is given by the critical manifold $\mathcal{C}_0$. Rescaling the traveling wave coordinate via $\tau = \varepsilon\xi$, we obtain the corresponding slow system

$$\begin{aligned} \varepsilon v' &= d \\ \varepsilon d' &= \frac{1}{D}\left(sd - f(v;\lambda) + w - p\right) \\ w' &= \frac{1}{s}\left(v - \gamma w\right) \end{aligned} \tag{5}$$

where $' = \frac{\mathrm{d}}{\mathrm{d}\tau}$. We note that the flow of (5) is identical to that of (3) for any $\varepsilon > 0$, but upon setting $\varepsilon = 0$, we obtain the reduced problem

$$\begin{aligned} 0 &= d \\ 0 &= \frac{1}{D}\left(sd - f(v;\lambda) + w - p\right) \\ w' &= \frac{1}{s}\left(v - \gamma w\right) \end{aligned} \tag{6}$$

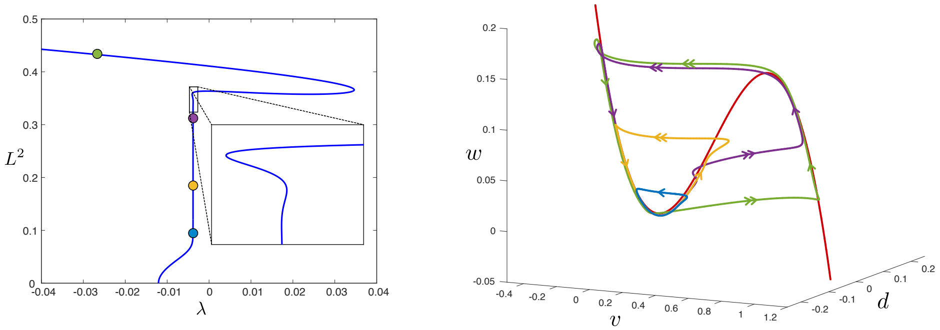

FIGURE 2. Plotted is the traveling canard explosion which emerges from the Hopf bifurcation at the equilibrium $(v, d, w) = (0, 0, 0)$ at the parameter values $p = 0$, $s = 0.65$, $\gamma = 0$, and $\varepsilon = 0.005$, when continuing in the parameter λ. The left panel shows the bifurcation diagram obtained by plotting the L^2-norm of the periodic orbits along the explosion vs. the parameter λ; a zoomed in portion of this bifurcation diagram showing the folds along the canard explosion is shown in the inset. The colored circles in the bifurcation diagram correspond to the periodic orbits in the right panel plotted in (v, d, w) phase space along with the cubic critical manifold (shown in red). The explosion encompasses the transition from small amplitude oscillations (blue) born locally at the Hopf bifurcation, to canards "without head" (yellow) and "with head" (purple), to large amplitude "relaxation oscillation"-type orbits (green). The folds in the bifurcation branch are observed primarily along the upper part of the branch, associated to the canards with head. We will discuss why these folds appear only on this part of the branch in §5.2.

for which the flow is restricted to the critical manifold $\mathcal{C}_0$. It is possible to build singular $\varepsilon = 0$ periodic orbits for (3) by concatenating solutions of the reduced problem (on the slow manifold $\mathcal{C}_0$) and the layer problem, which describes the fast dynamics away from $\mathcal{C}_0$.

We now examine the linear stability of the layer problem along the set of equilibria $\mathcal{C}_0 = \{d = 0, w = f(v; \lambda) - p\}$, which can be naturally parameterized by v. At a point $(v, d, w) = (v, 0, f(v; \lambda) - p) \in \mathcal{C}_0$, the linearization of (4) is given by

$$J(v, 0) \quad = \quad \begin{pmatrix} 0 & 1 \\ -\frac{f'(v;\lambda)}{D} & \frac{s}{D} \end{pmatrix} \tag{7}$$

The eigenvalues are then given by the following expression

$$\nu^{\pm} \quad = \quad \frac{1}{2}\left(\frac{s}{D} \pm \sqrt{\frac{s^2}{D^2} - 4\frac{f'(v;\lambda)}{D}}\right) \tag{8}$$

so that $\mathcal{C}_0$ is normally hyperbolic for any $s > 0$ except at two fold points $v = v_{\pm}^{\mathrm{f}}$ where

$$0 = f'(v; \lambda) = -3v_{\mathrm{f}}^2 + 2(1 + \lambda)v_{\mathrm{f}} - \lambda \tag{9}$$

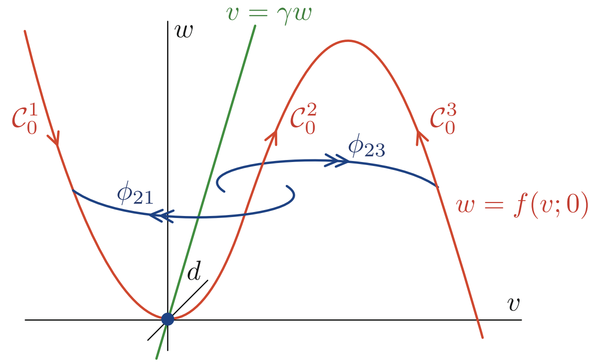

FIGURE 3. Shown the singular slow-fast geometry for the FitzHugh–Nagumo system (3) for $\lambda = \varepsilon = 0$.

that is,

$$v^{\mathrm{f}}_{\pm} = \frac{1}{3}\left((1+\lambda) \pm \sqrt{(1-\lambda)^2 - 3\lambda}\right). \tag{10}$$

This splits the manifold $\mathcal{C}_0$ into three normally hyperbolic branches

$$\mathcal{C}_0^1 = \mathcal{C}_0 \cap \{v < v^{\mathrm{f}}_-\}, \qquad \mathcal{C}_0^2 = \mathcal{C}_0 \cap \{v^{\mathrm{f}}_- < v < v^{\mathrm{f}}_+\}, \qquad \mathcal{C}_0^3 = \mathcal{C}_0 \cap \{v > v^{\mathrm{f}}_+\} \tag{11}$$

where the two outer branches $\mathcal{C}_0^1$ and $\mathcal{C}_0^3$ are of saddle type, and the middle branch $\mathcal{C}_0^2$ is normally repelling. Depending on the values of the parameters λ, s, D, for values of $w \in (f(v^{\mathrm{f}}_-; \lambda), f(v^{\mathrm{f}}_-; \lambda))$, between the fold points, there exists a family of heteroclinic orbits $\phi_{21}(\xi; w) = (v_{21}, d_{21})(\xi; w)$ and $\phi_{23}(\xi; w) = (v_{23}, d_{23})(\xi; w)$ which connect the repelling middle branch $\mathcal{C}_0^2$ with the outer saddle branches $\mathcal{C}_0^1$ and $\mathcal{C}_0^3$, respectively. For certain values of w, there are potentially also heteroclinic orbits $\phi_{13}(\xi; w) = (v_{13}, d_{13})(\xi; w)$ or $\phi_{31}(\xi; w) = (v_{31}, d_{31})(\xi; w)$ which connect the outer branches $\mathcal{C}_0^1$ and $\mathcal{C}_0^3$, or vice versa. We refer to [6, Figure 2] for a qualitative description of the possible phase portraits of (4) in the case $D = 1, p = 0$ for different values of λ and s.

Examining the reduced flow (6) restricted to the critical manifold $\mathcal{C}_0$, we note that the direction of flow is determined by the nullcline $v = \gamma w$; see Figure 3. When $\lambda = 0$, the equilibrium $(v, d, w) = (0, 0, 0)$ sits at the lower left fold point, which in the singular limit $\varepsilon \to 0$ takes the form of a canard point. Singular periodic orbits can be formed by concatenating canard orbits which follow the saddle critical manifold $\mathcal{C}_0^1$ then the repelling middle branch $\mathcal{C}_0^2$, followed by one of the fast heteroclinic orbits $\phi_{21}(\cdot; w)$ or $\phi_{23}(\cdot; w)$. Following one of the orbits $\phi_{21}(\cdot; w)$ back to the saddle branch $\mathcal{C}_0^1$ results in a singular canard "without head"; however, if following $\phi_{21}(\cdot; w)$, the orbit jumps to the right saddle branch $\mathcal{C}_0^3$ and continues to the upper right fold point before returning to the left saddle branch $\mathcal{C}_0^1$, forming a singular canard "with head".

In the forthcoming analysis, we will show that the sequence of folds in the bifurcation branch that undergoes a canard explosion in Figure 2 is related to the small amplitude oscillations made by the canard orbits about the middle branch $\mathcal{C}_0^2$ of the critical manifold; these can be seen along the canard orbits in phase space in Figure 2. These oscillations arise along a portion of the repelling middle branch $\mathcal{C}_0^2$ in which the associated equilibria of the fast subsystem transition from repelling nodes to foci in the layer problem. From (8), the condition to have foci is

$$\frac{s^2}{D^2} - 4\frac{f'(v;\lambda)}{D} < 0 \tag{12}$$

or equivalently,

$$3v^2 - 2(\lambda+1)v + \lambda + \frac{s^2}{4D} < 0 \tag{13}$$

The equality in equation (13) gives a quadratic equation whose roots are

$$v_\pm \;=\; \frac{1}{3}\left(1+\lambda \pm \sqrt{(1+\lambda)^2 - 3\left(\lambda + \frac{s^2}{4D}\right)}\right), \tag{14}$$

Then, provided

$$(1+\lambda)^2 - 3\left(\lambda + \frac{s^2}{4D}\right) > 0 \tag{15}$$

equation (13) has solutions on $v \in (v_-, v_+)$, and we refer to the points $(v_\pm, w_\pm) = (v_\pm, f(v_\pm;\lambda))$ at which the node-to-focus transition occurs as Airy points [5]. Comparing (14) and (10), we can conclude that, for values of λ, s satisfying (15), the solutions to the inequality (13) lie on the middle (repelling) branch of the cubic critical manifold, where the equilibria (of the fast subsystem) are then foci. In particular, for $\lambda = 0$ and $0 < s < \frac{2D}{\sqrt{3}}$, there exists a portion of $\mathcal{C}_0^2$ with this focus structure, and any canard orbits passing near this portion of slow manifold will exhibit small oscillations around $\mathcal{C}_0^2$.

The aim of this paper is to show that, under suitable assumptions, these oscillations organize the folds in the bifurcation curve in Figure 2, and we will obtain asymptotic estimates for the location and number of these folds in the singular limit $\varepsilon \to 0$. After construction of a general theory, we will return to the FitzHugh–Nagumo system in §5.2 and show how it fits into this framework.

3. A normal form for wiggly canards.

Motivated by the geometry of the FitzHugh–Nagumo system in the previous section, we consider a 2-fast-1-slow system with fast variables (v, d), slow variable w, which we write in the form

$$\begin{aligned} \dot{v} &= g_1(v,d,w,\lambda,\varepsilon) \\ \dot{d} &= g_2(v,d,w,\lambda,\varepsilon) \\ \dot{w} &= \varepsilon h(v,d,w,\lambda,\varepsilon), \end{aligned} \tag{16}$$

where $\dot{} = \frac{\mathrm{d}}{\mathrm{d}\xi}$, λ is a bifurcation parameter, $\varepsilon > 0$ is a small parameter and g_1, g_2, h are C^{r+1} functions, $r \geq 3$. By rescaling $\tau = \varepsilon t$, we obtain the corresponding slow system

$$\begin{aligned} \varepsilon v' &= g_1(v,d,w,\lambda,\varepsilon) \\ \varepsilon d' &= g_2(v,d,w,\lambda,\varepsilon) \\ w' &= h(v,d,w,\lambda,\varepsilon), \end{aligned} \tag{17}$$

where $' = \frac{\mathrm{d}}{\mathrm{d}\tau}$. We outline hypotheses with respect to the slow/fast limits in §3.1. Also see Figure 4.

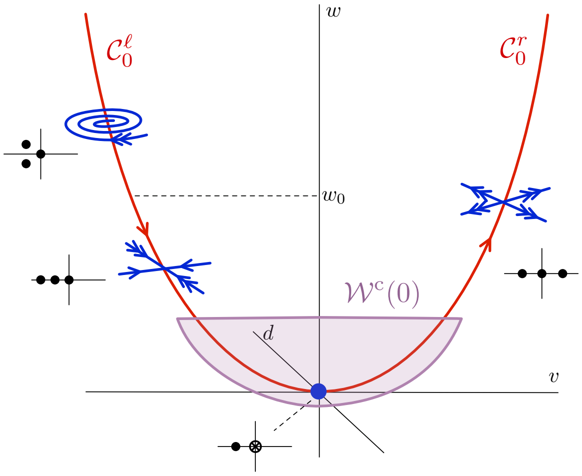

FIGURE 4. The global setup of the slow-fast system (16) according to Hypotheses 1-4. For convenience the origin is taken to coincide with the fold point $\mathcal{F} = (v_{\mathrm{f}}, d_{\mathrm{f}}, w_{\mathrm{f}})$.

3.1. **Fast and slow limits.** Setting $\varepsilon = 0$ in (16) results in the *layer problem*

$$\begin{aligned} \dot{v} &= g_1(v, d, w, \lambda, 0) \\ \dot{d} &= g_2(v, d, w, \lambda, 0) \\ \dot{w} &= 0, \end{aligned} \tag{18}$$

which we consider for $\lambda \in [-\lambda_0, \lambda_0]$ for some $\lambda_0 > 0$. The dynamics are restricted to planes $w =$const, and this system admits a critical manifold of equilibria

$$\mathcal{C}_0 := \{(v, d, w) : F(v, d, w, \lambda, 0) = 0\}, \qquad F(v, d, w, \lambda, \varepsilon) := \begin{pmatrix} g_1(v, d, w, \lambda, \varepsilon) \\ g_2 v, d, w, \lambda, \varepsilon) \end{pmatrix} \tag{19}$$

We assume that for $w > w_{\mathrm{f}}$, (18) admits two hyperbolic fixed points: $p_\ell(w)$, and $p_r(w)$, and these collide at a saddle-node bifurcation at $w = w_{\mathrm{f}}$. In other words, we assume that the critical manifold is folded, or U-shaped with two normally hyperbolic branches $\mathcal{C}_0^\ell, \mathcal{C}_0^r$ and single fold point at

$$\mathcal{F} = (v_{\mathrm{f}}, d_{\mathrm{f}}, w_{\mathrm{f}}). \tag{20}$$

so that

$$\mathcal{C}_0 = \mathcal{C}_0^\ell \cup \mathcal{F} \cup \mathcal{C}_0^r. \tag{21}$$

Regarding the stability of the hyperbolic branches of the critical manifold, we have

Hypothesis 1. The left and right branches of the critical manifold $\mathcal{C}_0$ satisfy the following.

(i) The left branch $\mathcal{C}_0^\ell$ is normally attracting, that is, $D_{(v,d)}F|_{\mathcal{C}_0^\ell}$ has two eigenvalues with negative real part. There exists $w_0 > w_{\mathrm{f}}$ such that for $w_{\mathrm{f}} < w < w_0$, these two eigenvalues are real and denoted by $\nu_\ell^\pm(w)$, where $\nu_\ell^- < \nu_\ell^+ < 0$, while for $w > w_0$, the eigenvalues are complex with $\nu_\ell^\pm(w) = -\alpha(w) \pm i\omega(w)$,

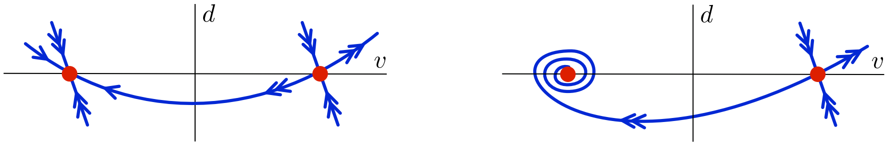

FIGURE 5. The assumed heteroclinic orbits in the layer problem according to Hypothesis 2 in the case $w < w_0$ (left) and $w > w_0$ (right). In the left panel, the heteroclinic orbits $\phi(w)$ are shown to converge to $\mathcal{C}_0^\ell$ in the generic (weak stable) direction, as is the case for the FitzHugh–Nagumo system (3), but this is not necessary to satisfy Hypothesis 2 for the construction of periodic orbits.

where $\alpha(w), \omega(w) > 0$ for $w > w_0$. The double root $\nu_\ell^+(w_0) = \nu_\ell^-(w_0)$ is geometrically simple.

(ii) The right branch $\mathcal{C}_0^r$ is of saddle type, so that $D_{(v,d)}F|_{\mathcal{C}_0^r}$ has one positive and one negative eigenvalue, denoted $\nu_r^\pm(w)$.

We refer to the equilibrium $p_\ell(w_0)$ at which the fast dynamics transitions from node to focus as an Airy point. The next hypothesis concerns the existence of heteroclinic orbits connecting the right branch $\mathcal{C}_0^r$ to the left branch $\mathcal{C}_0^\ell$. See Figure 5.

Hypothesis 2. (Behavior of $\mathcal{W}^{\mathrm{u}}(\mathcal{C}_0^r)$) For each value of $w > w_{\mathrm{f}}$, the saddle equilibrium $p_r(w)$ has a one dimensional unstable manifold $\mathcal{W}^{\mathrm{u}}(p_r(w))$ which is composed of two orbits W_-^r, W_+^r. For each $w > w_{\mathrm{f}}$, W_-^r is given by a heteroclinic orbit $\phi(w)$ which crosses the set $\{v = v_{\mathrm{f}}\}$ transversely and limits onto the stable equilibrium $p_\ell(w)$ on the left branch $\mathcal{C}_0^\ell$.

Taking $\varepsilon = 0$ in (17) results in the associated *reduced problem*

$$\begin{aligned} 0 &= g_1(v, d, w, \lambda, 0) \\ 0 &= g_2(v, d, w, \lambda, 0) \\ w' &= h(v, d, w, \lambda, 0), \end{aligned} \tag{22}$$

which we assume satisfies the following.

Hypothesis 3. (Slow flow). The function $h_0(v, d, w) = h(v, d, w, 0, 0)$ satisfies

$$h_0|_{\mathcal{C}_0^\ell} < 0, \qquad h_0|_{\mathcal{C}_0^r} > 0, \qquad h_0(v_{\mathrm{f}}, d_{\mathrm{f}}, w_{\mathrm{f}}) = 0. \tag{23}$$

Remark 2. We note that in the case of the FitzHugh–Nagumo system (3), the manifolds $\mathcal{C}_0^1$ and $\mathcal{C}_0^2$ correspond to $\mathcal{C}_0^r$ and $\mathcal{C}_0^\ell$, respectively under the reversal $\xi \to -\xi$ (note that the left/right orientation of $\mathcal{C}_0^1$ and $\mathcal{C}_0^2$ in Figure 3 is flipped compared to that of $\mathcal{C}_0^r$ and $\mathcal{C}_0^\ell$ in Figure 4). See 5.2 for further details.

Finally we discuss the dynamics near the nonhyperbolic fold point $\mathcal{F}$. We have the following (see Figure 4).

Hypothesis 4. (Normally attracting canard point) The point $\mathcal{F}$ is a normally attracting canard point, that is,

$$D_{(v,d)}F(v_{\mathrm{f}}, d_{\mathrm{f}}, w_{\mathrm{f}}, \lambda, 0) \tag{24}$$

has one negative eigenvalue for $\lambda \in [-\lambda_0, \lambda_0]$. Therefore (16) admits a two-dimensional local center manifold $\mathcal{W}^{\mathrm{c}}(\mathcal{F})$, on which we assume the point $\mathcal{F}$ is a nondegenerate canard point with unfolding parameter λ in the sense of [25, §3.1].

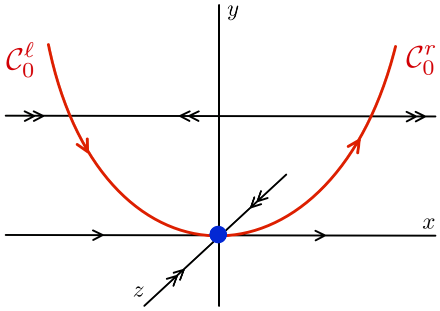

FIGURE 6. Shown is the setup for Hypothesis 4 in the local coordinates (x, y, z) for the normal form (25) for $\varepsilon = 0$.

Hypothesis 4 implies the existence of a local invariant manifold $\mathcal{W}^{\mathrm{c}}(\mathcal{F})$, foliated by one-dimensional strong stable fibers. In a local coordinate system (x, y, z), where (x, y) parameterize the center manifold, and z parameterizes the transverse direction (see Figure 6), after a suitable coordinate transformation, we arrive at the following normal form for a canard point [25]

$$\begin{aligned}\dot{x} &= -yh_1(x,y,\lambda,\varepsilon) + x^2h_2(x,y,\lambda,\varepsilon) + \varepsilon h_3(x,y,\lambda,\varepsilon)\\ \dot{y} &= \varepsilon\left(xh_4(x,y,\lambda,\varepsilon) - \lambda h_5(x,y,\lambda,\varepsilon) + yh_6(x,y,\lambda,\varepsilon)\right)\\ \dot{z} &= z\left(-k(\lambda) + \mathcal{O}(x,y,z,\varepsilon)\right)\end{aligned} \tag{25}$$

where $k(\lambda) > 0$, and the functions $h_j, j = 1, \ldots, 6$ are C^r and satisfy

$$\begin{aligned}h_3(x,y,\lambda,\varepsilon) &= \mathcal{O}(x,y,\lambda,\varepsilon)\\ h_j(x,y,\lambda,\varepsilon) &= 1 + \mathcal{O}(x,y,\lambda,\varepsilon), \quad j = 1,2,4,5.\end{aligned} \tag{26}$$

By standard planar canard theory [26], this system admits a Hopf bifurcation at

$$\lambda = \lambda_H(\sqrt{\varepsilon}) = -\frac{1}{2}K_H\varepsilon + \mathcal{O}(\varepsilon^{3/2}), \tag{27}$$

where $K_H := \partial_x h_3(0,0,0,0) + h_6(0,0,0,0)$, which can be either sub- or supercritical, depending on certain higher order coefficients in (25); see [26, Theorem 3.1]. From this Hopf curve bifurcates a family of periodic orbits, given by small amplitude canard cycles, which grow to small, but $\mathcal{O}(1)$ with respect to ε, size within the center manifold $\mathcal{W}^{\mathrm{c}}(\mathcal{F})$; this constitutes the so-called "local canard explosion" phenomenon. In particular, by taking $\Delta > 0$ sufficiently small, one can guarantee that for all sufficiently small $\varepsilon > 0$, this family of canard cycles leaves a Δ-neighborhood of the fold point $(v, d, w) = (v_{\mathrm{f}}, d_{\mathrm{f}}, w_{\mathrm{f}})$. However, this local result is restricted to those orbits which are entirely contained in the center manifold $\mathcal{W}^{\mathrm{c}}(\mathcal{F})$, and in particular does not extend to the region of interest $w > w_0$. The center manifold $\mathcal{W}^{\mathrm{c}}(\mathcal{F})$ cannot be continued beyond the Airy point at $w = w_0$ due to the lack of a spectral gap in the eigenvalues $\nu_\ell^{\pm}(w)$ for $w > w_0$. To understand orbits which interact with the fast foci on $\mathcal{C}_0^\ell$, we must understand the structure of global canard orbits which leave $\mathcal{W}^{\mathrm{c}}(\mathcal{F})$.

3.2. **"Global" canard cycles.** To construct global canard cycles, which are not fully contained in the center manifold $\mathcal{W}^{\mathrm{c}}(\mathcal{F})$, we must examine the flow away from the fold point, and in particular, the full three-dimensional nature of the flow becomes important. We follow the procedure used in [2] for constructing such global canard orbits.

For $w_1, w_2 > w_{\mathrm{f}}$, we use the notation $\mathcal{C}_0^*[w_1, w_2]$, $* = \ell, r$ to denote the intersection

$$\mathcal{C}_0^*[w_1, w_2] := \mathcal{C}_0^* \cap \{w_1 \leq w \leq w_2\}. \tag{28}$$

For each $w = \bar{w} > w_{\mathrm{f}}$, we can construct a periodic orbit as a perturbation of the singular $\varepsilon = 0$ orbit $\gamma_0(\bar{w})$ obtained by traversing the left critical manifold $\mathcal{C}_0^\ell[w_{\mathrm{f}}, \bar{w}]$, continuing up the right critical manifold $\mathcal{C}_0^r[w_{\mathrm{f}}, \bar{w}]$, then jumping back across the heteroclinic orbit $\phi(\bar{w})$, completing a cycle; a corresponding canard orbit $\gamma(\bar{w}; \varepsilon)$ for $0 < \varepsilon \ll 1$ can be constructed by perturbing from this singular cycle and adjusting the parameter $\lambda = \lambda(\bar{w}; \varepsilon)$ appropriately. We have the following.

Theorem 3.1. *([2, §3]) Consider (16) under Hypotheses 1-4. Fix $\bar{w}_m > w_{\mathrm{f}}$ and $\Delta > 0$ sufficiently small. There exists $\varepsilon_0, \eta > 0$, $\mu \neq 0$, and a family of locally unique periodic orbits*

$$\{(\gamma(\bar{w}; \varepsilon), \lambda(\bar{w}; \varepsilon)) : \bar{w} \in (w_{\mathrm{f}} + \Delta, \bar{w}_m), \varepsilon \in (0, \varepsilon_0)\} \tag{29}$$

which is C^1 in $(\bar{w}, \sqrt{\varepsilon})$. The function $\lambda(\bar{w}; \varepsilon)$ satisfies

$$\lambda(\bar{w}; \varepsilon) = \lambda^{\mathrm{mc}}(\varepsilon) + \mathcal{O}\left(e^{-\eta/\varepsilon}\right) \tag{30}$$

uniformly in $\bar{w} \in (w_{\mathrm{f}} + \Delta, \bar{w}_m)$ and $\varepsilon \in (0, \varepsilon_0)$ where

$$\lambda^{\mathrm{mc}}(\varepsilon) = \mu\varepsilon + \mathcal{O}\left(\varepsilon^{3/2}\right). \tag{31}$$

The orbit $\gamma(\bar{w}; \varepsilon)$ intersects the section $\{v = v_{\mathrm{f}}\}$ at $w = \bar{w}$ and is $\mathcal{O}(\sqrt{\varepsilon})$-close to the singular orbit $\gamma_0(\bar{w})$.

Remark 3. Due to local uniqueness, by taking $\Delta > 0$ sufficiently small, we can guarantee that for $\bar{w} \approx w_{\mathrm{f}} + \Delta$, the orbits $\gamma(\bar{w}; \varepsilon)$ coincide with those arising from the local canard explosion as in §3.1, forming a single continuous branch originating at the Hopf bifurcation (27).

Remark 4. The function $\lambda_{\mathrm{mc}}(\varepsilon)$ which appears in the estimate (29) represents the location of the so-called maximal canard orbit. All of the periodic orbits of Theorem 3.1 lie within an exponentially thin interval of this value in parameter space.

The existence of the periodic orbits of Theorem 3.1 follows from the analysis in [2, §3.5]. However, below we include a self-contained proof of Theorem 3.1 in order to explain the origin and geometry of the leading order bifurcation equations, which will be essential in obtaining the formal asymptotic predictions in §4.

3.2.1. *Setup for constructing global orbits.* From standard results of geometric singular perturbation theory, away from the fold point, the normally hyperbolic branches $\mathcal{C}_0^{r/\ell}$ of the critical manifold perturb to one-dimensional slow manifolds $\mathcal{C}_\varepsilon^{r/\ell}$ for sufficiently small $\varepsilon > 0$. Furthermore, the three-dimensional stable manifold $\mathcal{W}^{\mathrm{s}}(\mathcal{C}_0^\ell)$ of the left branch perturbs to a locally invariant three dimensional stable manifold $\mathcal{W}^{\mathrm{s}}(\mathcal{C}_\varepsilon^\ell)$ of the slow manifold $\mathcal{C}_\varepsilon^\ell$. Similarly the two-dimensional stable/unstable manifolds $\mathcal{W}^{\mathrm{s/u}}(\mathcal{C}_0^r)$ of the saddle manifold $\mathcal{C}_0^r$ perturb for small $\varepsilon > 0$ to two-dimensional locally invariant stable/unstable manifolds $\mathcal{W}^{\mathrm{s/u}}(\mathcal{C}_\varepsilon^r)$ of the saddle slow manifold $\mathcal{C}_\varepsilon^r$.

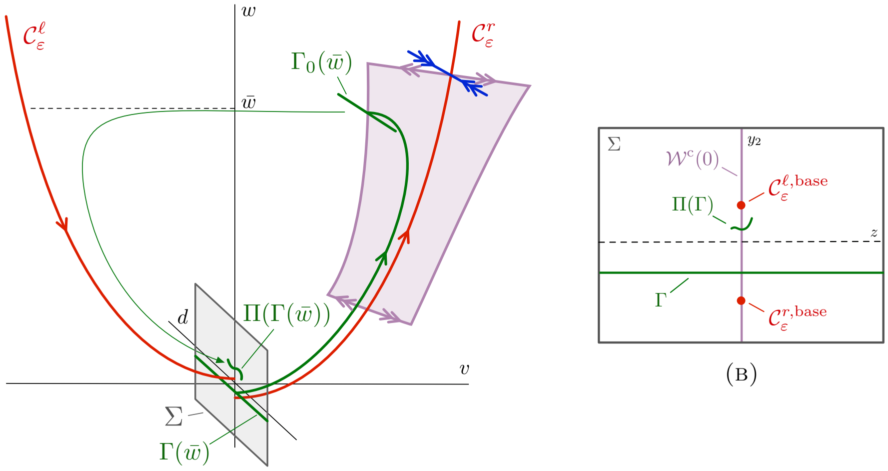

(A)

(B)

FIGURE 7. (a) Geometric setup for the construction of global canard orbits as in Theorem 3.1. (b) Setup for matching conditions in the section Σ.

Due to the existence of the heteroclinic orbits $\phi(w) \subset \mathcal{W}^{\mathrm{s}}(\mathcal{C}_0^\ell) \cap \mathcal{W}^{\mathrm{u}}(\mathcal{C}_0^r)$ for $\varepsilon = 0$, away from the fold point $\mathcal{F}$, tracking the unstable manifold $\mathcal{W}^{\mathrm{u}}(\mathcal{C}_\varepsilon^r)$ forwards, we note that $\mathcal{W}^{\mathrm{u}}(\mathcal{C}_\varepsilon^r) \subset \mathcal{W}^{\mathrm{s}}(\mathcal{C}_\varepsilon^\ell)$.

To construct the orbits of Theorem 3.1, we consider a small one-dimensional manifold $\Gamma_0(\bar{w})$ lying entirely in the plane $w = \bar{w}$ which transversely intersects the heteroclinic orbit $\phi(\bar{w})$; see Figure 7a. This one dimensional manifold therefore transversely intersects $\mathcal{W}^{\mathrm{u}}(\mathcal{C}_\varepsilon^r)$. To construct a periodic orbit which reaches $w = \bar{w}$, we evolve $\Gamma_0(\bar{w})$ under the forwards and backwards flow of (16), and search for intersections near the fold point $\mathcal{F}$, through a matching analysis using the local coordinates (x, y, z).

Under the forwards flow of (16), $\Gamma_0(\bar{w})$ is contracted exponentially close to the manifold $\mathcal{C}_\varepsilon^\ell$, arriving in a small neighborhood of the fold point. Under the reverse flow of (16), since $\Gamma_0(\bar{w})$ transversely intersects $\mathcal{W}^{\mathrm{u}}(\mathcal{C}_\varepsilon^r)$, by the exchange lemma (see [22]) $\Gamma_0(\bar{w})$ traces out a two-dimensional manifold $\widehat{\Gamma}_0(\bar{w})$ which aligns $\mathcal{O}(e^{-\eta/\varepsilon})$-close to $\mathcal{W}^{\mathrm{s}}(\mathcal{C}_\varepsilon^r)$ upon arriving in a neighborhood of the fold point, for some $\eta > 0$ fixed independently of ε.

3.2.2. *Matching analysis near the canard point.* We recall that the flow near the canard point is governed by (25) in the local (x, y, z)-coordinate system. We fix a Poincaré section given by the set $\Sigma := \{x = 0\}$ and proceed to define a suitable return map on this set in order to construct canard cycles; see Figure 7b.

We note that the (non-unique) slow manifolds $\mathcal{C}_\varepsilon^{r/\ell}$ themselves (in particular $\mathcal{C}_\varepsilon^r$) cannot be tracked inside an arbitrarily small neighborhood of the fold point, due to the normally attracting direction transverse to the local center manifold of the fold. However, given any fixed small $\mathcal{O}(1)$ neighborhood of the fold in which the center manifold $\mathcal{W}^{\mathrm{c}}(\mathcal{F})$ is defined, the slow manifolds $\mathcal{C}_\varepsilon^{r/\ell}$ can be tracked up to the boundary of this neighborhood. Upon reaching this neighborhood, there are corresponding basepoint solutions $\mathcal{C}_\varepsilon^{\ell,\mathrm{base}}$ and $\mathcal{C}_\varepsilon^{r,\mathrm{base}}$, which lie on $\mathcal{W}^{\mathrm{c}}(\mathcal{F})$, which

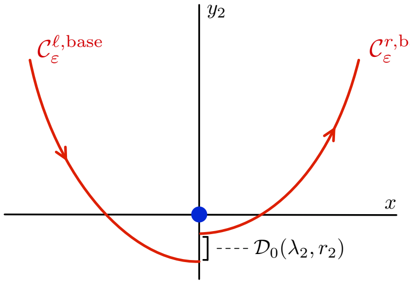

FIGURE 8. Splitting of the manifolds $\mathcal{C}_\varepsilon^{\ell,\mathrm{base}}$ and $\mathcal{C}_\varepsilon^{\ell,\mathrm{base}}$ in the center manifold $\mathcal{W}^{\mathrm{c}}(\mathcal{F})$.

are shadowed by the slow manifolds $\mathcal{C}_\varepsilon^{r/\ell}$. The behavior of these basepoint solutions can then be analyzed using standard planar canard analysis [25, 26].

Within the center manifold, the shadowed slow-manifolds $\mathcal{C}_\varepsilon^{\ell,\mathrm{base}}$ and $\mathcal{C}_\varepsilon^{r,\mathrm{base}}$ can be tracked down to the fold, where they meet the section Σ within the subspace $z = 0$. The distance between these solutions can be measured using blow-up analysis. In particular, via the blow-up transformation

$$x = r_2 x_2, \quad y = r_2^2 y_2, \quad \lambda = r_2\lambda_2, \quad \varepsilon = r_2^2. \tag{32}$$

the manifolds $\mathcal{C}_\varepsilon^{\ell,\mathrm{base}}$ and $\mathcal{C}_\varepsilon^{r,\mathrm{base}}$ reach Σ in the subspace $z = 0$ at $y_2 = y_2^\ell(\lambda_2, r_2)$ and $y_2 = y_2^r(\lambda_2, r_2)$, respectively; further, we have that the distance between $\mathcal{C}_\varepsilon^{\ell,\mathrm{base}}$ and $\mathcal{C}_\varepsilon^{r,\mathrm{base}}$ measured in the section Σ is given by the distance function [25, Proposition 3.5]

$$y_2^\ell - y_2^r = \mathcal{D}_0(\lambda_2, r_2) = m_1\lambda_2 + m_2 r_2 + \mathcal{O}(r_2^2 + \lambda_2^2)\ , \tag{33}$$

where the coefficients m_1, m_2 are constants, bounded away from zero independently of λ_2, r_2. Hence we can solve for the existence of a maximal canard trajectory within $\mathcal{W}^{\mathrm{c}}(\mathcal{F})$, corresponding to a zero of the distance function $\mathcal{D}_0(\lambda_2, r_2)$, which occurs when

$$\lambda_2 = \lambda_2^{\mathrm{mc}} = \mu r_2 + \mathcal{O}(r_2^2), \tag{34}$$

where $\mu = -\frac{m_2}{m_1} \neq 0$, and the corresponding λ value of $\lambda^{\mathrm{mc}} = r_2\lambda_2^{\mathrm{mc}}$; see Figure 8.

Using these blow up coordinates, we can now complete the proof of Theorem 3.1.

Proof of Theorem 3.1. In order to construct the desired family of periodic orbits, we determine appropriate estimates on the return map $\Pi : \Sigma \to \Sigma$ applied to $\Gamma(\bar{w})$. We first note that by the discussion above, the manifolds $\mathcal{C}_\varepsilon^{\ell,\mathrm{base}}$ and $\mathcal{C}_\varepsilon^{r,\mathrm{base}}$ intersect Σ at

$$\begin{aligned} \mathcal{C}_\varepsilon^{\ell,\mathrm{base}} &: (y, z) = (y_2^\ell, 0) \\ \mathcal{C}_\varepsilon^{r,\mathrm{base}} &: (y, z) = (y_2^r, 0). \end{aligned} \tag{35}$$

Next, we consider the backwards evolution of the set $\Gamma_0(\bar{w})$. As already mentioned, because $\Gamma_0(\bar{w})$ transversely intersects $\mathcal{W}^{\mathrm{u}}(\mathcal{C}_\varepsilon^r)$, by the exchange lemma (see [22]) $\Gamma_0(\bar{w})$ traces out a two dimensional manifold $\widehat{\Gamma}_0(\bar{w})$ which aligns exponentially close to $\mathcal{W}^{\mathrm{s}}(\mathcal{C}_\varepsilon^r)$, and hence transversely intersects the center manifold $\mathcal{W}^{\mathrm{c}}(\mathcal{F})$. Thus in backwards time, $\widehat{\Gamma}_0(\bar{w})$ aligns exponentially close to the strong stable fibers of a basepoint solution on $\mathcal{W}^{\mathrm{c}}(\mathcal{F})$ which is exponentially close to $\mathcal{C}_\varepsilon^{r,\mathrm{base}}$ upon arrival in the section Σ.

Hence $\widehat{\Gamma}_0(\bar{w})$ intersects Σ in a curve $\Gamma(\bar{w})$ which can be represented as a graph over z for $|z| \leq \Delta$, for some $\Delta > 0$

$$\Gamma(\bar{w}) : y_2 = y_\Gamma(z; \bar{w}), \quad |z| \leq \Delta \tag{36}$$

where

$$y_\Gamma(0; \bar{w}) = y_2^r + \mathcal{O}(e^{-\eta/\varepsilon}), \qquad (y_\Gamma)'(0; \bar{w}) = \mathcal{O}(e^{-\eta/\varepsilon}). \tag{37}$$

We now consider the image of $\Gamma(\bar{w})$ under the return map Π. In forwards time, $\Gamma(\bar{w})$ is contracted exponentially, occupying an exponentially thin interval within the original manifold $\Gamma_0(\bar{w})$, which is then itself exponentially contracted to $\mathcal{C}_\varepsilon^\ell$, and hence arrives back in Σ in a curve $\Pi(\Gamma(\bar{w}))$ which is contracted exponentially close to $\mathcal{C}_\varepsilon^{\ell,\text{base}}$. We parameterize this curve by $|s| \leq \Delta$ where s denotes the initial z-coordinate of a point on $\Gamma(\bar{w})$ within the section Σ before applying the map Π. Hence $\Pi(\Gamma(\bar{w}))$ is given by

$$\Pi(\Gamma(\bar{w})) : (y_2, z) = (y_\Pi(s; \bar{w}), z_\Pi(s; \bar{w})) \quad |s| \leq \Delta \tag{38}$$

where

$$y_\Pi(s; \bar{w}) = y_2^\ell + \mathcal{O}(e^{-\eta/\epsilon}), \qquad z_\Pi(s; \bar{w}) = \mathcal{O}(e^{-\eta/\epsilon}) \tag{39}$$

uniformly in s, w, λ_2, and the derivatives of these functions with respect to s, w, λ_2 satisfy the same estimates.

To find a periodic orbit, we search for a fixed point of Π on the set $\Gamma(\bar{w})$, that is, we search for a value of $|s| \leq \Delta$ such that

$$y_\Gamma(z_\Pi(s; \bar{w}); \bar{w}) = y_\Pi(s; \bar{w}). \tag{40}$$

Using the estimates (37) and (39), we can write this as

$$\begin{aligned} 0 &= y_\Pi(s; \bar{w}) - y_\Gamma(z_\Pi(s; \bar{w}); \bar{w}) \\ &= y_2^\ell + \mathcal{O}(e^{-\eta/\epsilon}) - y_2^r + \mathcal{O}(e^{-\eta/\epsilon}) \\ &= \mathcal{D}_0(\lambda_2, r_2) + \mathcal{O}(e^{-\eta/\epsilon}), \end{aligned}$$

where $\mathcal{D}_0$ is as in (33) which can be solved for

$$\lambda_2 = \lambda_2(r_2; \bar{w}) = \lambda_2^{\text{mc}} + \mathcal{O}(e^{-\eta/\epsilon}) = \mu r_2 + \mathcal{O}(r_2^2), \tag{41}$$

by the implicit function theorem, where we recall that $\lambda = r_2\lambda_2$, where $r_2 = \varepsilon^{1/2}$. This gives the value of $\lambda(\bar{w}; \varepsilon) = r_2\lambda_2(r_2; \bar{w})$ for which there exists a canard cycle, which we call $\gamma(\bar{w}; \varepsilon)$, which reaches $w = \bar{w}$. □

Remark 5. We note that the above procedure for constructing $\mathcal{O}(1)$ canard orbits can be employed for more general situations, beyond the case in which the critical manifold has the parabolic shape as depicted in Figure 4. For instance, in the case of a cubic critical manifold, as in the FitzHugh–Nagumo system (3), Theorem 3.1 applies directly to the construction of the so-called canard orbits "without head", but does not include the canard orbits "with head", which traverse the right saddle branch and upper right fold point before returning to the canard point along the left saddle branch. These can, however, be constructed similarly by choosing an appropriate interval of initial conditions, and showing that any exponential expansion along the right slow manifold is balanced by contraction along the left slow manifold; see [5, §4] for a similar construction.

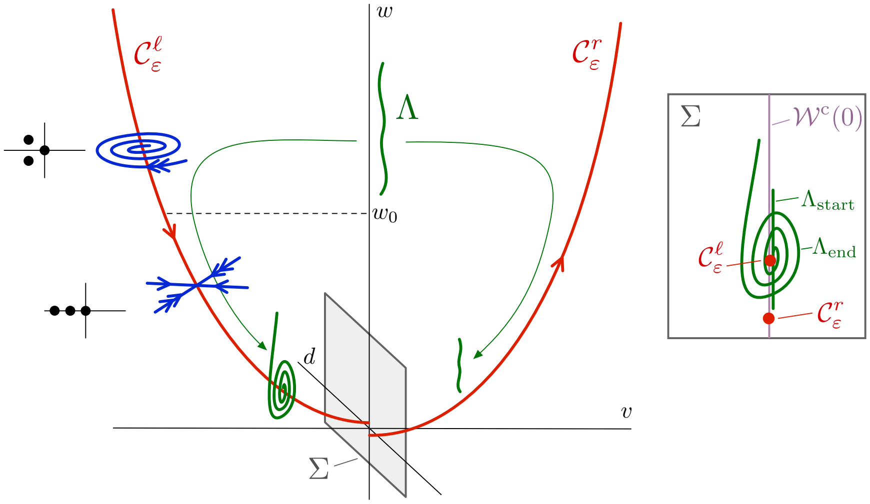

FIGURE 9. Shown is the forward/backward evolution of the curve Λ along the manifolds $\mathcal{C}_\varepsilon^{\ell,r}$. The right panel shows the forward and backwards intersections $\Lambda_{\text{start}}, \Lambda_{\text{end}}$ of Λ with the section Σ. The rotation along the left branch is accumulated in the region $w > w_0$ where the fast dynamics along $\mathcal{C}_\varepsilon^\ell$ are oscillatory.

4. Wiggly canard explosion and asymptotic predictions.

In this section, we use the analysis in §3.2 to make predictions about the appearance of wiggles, or folds, in the continuation of canard orbits from Theorem 3.1 in the bifurcation parameter λ. We begin with a discussion in §4.1 of the asymptotics of the parameter λ itself as well as a condition which predicts the appearance of folds. We then consider the asymptotics of the distance between successive folds in §4.2–4.3.

4.1. λ-aymptotics.

In §3.2, for sufficiently small $\varepsilon > 0$, we showed that for each $\bar{w} > w_{\text{f}}$, there exists a locally unique $\lambda = \lambda(\bar{w}; \varepsilon)$ and corresponding periodic orbit $\gamma(\bar{w}; \varepsilon)$ which reaches $w = \bar{w}$. We now aim to determine the asymptotics of $\lambda(\bar{w}; \varepsilon)$ as $\varepsilon \to 0$, in particular with respect to wiggling.

To do this, we consider the intersection of $\gamma(\bar{w}; \varepsilon)$ with the set $\{v = 0\}$ for a range of $\bar{w} > w_{\text{f}}$; this forms a curve, which we call Λ; see Figure 9. We now consider the backward evolution of Λ, which meets the section Σ in a curve Λ_{start}, as well as its forward evolution, which meets the section Σ in a curve Λ_{end}. When $\lambda = \lambda(\bar{w}; \varepsilon)$, we have a fixed point along the orbit $\gamma(\bar{w}; \varepsilon)$ which lies on the intersection of Λ_{start} and Λ_{end} within the section Σ. We argue below that the curve Λ_{end} oscillates about $\mathcal{C}_\varepsilon^\ell$, forming a spiral, and as $\lambda(\bar{w}; \varepsilon)$ adjusts for increasing $\bar{w}$, this fixed point travels deeper into the spiral; see Figure 9.

We now recall the local coordinates (y_2, z) used for matching in §3.2.2. In these coordinates, we have that the curves $\Lambda_{\text{start}}, \Lambda_{\text{end}}$ can be parameterized by $\bar{w}$:

$$\begin{aligned} \Lambda_{\text{start}} &: (y_2, z) = (y_{\text{start}}, z_{\text{start}})(\bar{w}) \\ \Lambda_{\text{end}} &: (y_2, z) = (y_{\text{end}}, z_{\text{end}})(\bar{w}), \end{aligned} \tag{42}$$

and when $\lambda = \lambda(\bar{w})$, we have that $y_{\text{start}}(\bar{w}) = y_{\text{end}}(\bar{w})$, which means

$$0 = y_{\text{start}}(\bar{w}) - y_{\text{end}}(\bar{w})$$

$$
\begin{aligned}
&= y_2^\ell + (y_{\text{start}} - y_2^\ell) - y_2^r + (y_2^r - y_{\text{end}}) \\
&= \mathcal{D}_0(\lambda_2, r_2) + (y_{\text{start}} - y_2^\ell) + (y_2^r - y_{\text{end}}).
\end{aligned}
$$

We recall that that $\mathcal{D}_0(\lambda_2, r_2) = 0$ (i.e. the maximal canard occurs) when $\lambda_2 = \lambda_2^{\text{mc}}$. We now set $\lambda_2 = \lambda_2^{\text{mc}} + \tilde{\lambda}$, and expand

$$
\mathcal{D}_0(\lambda_2^{\text{mc}} + \tilde{\lambda}, r_2) = m_1\tilde{\lambda} + \mathcal{O}(\tilde{\lambda}^2, r_2\tilde{\lambda}) \tag{43}
$$

From this, we deduce that the orbit $\gamma(\bar{w};\varepsilon)$ occurs for the value of $\tilde{\lambda} = \tilde{\lambda}(\bar{w})$ satisfying

$$
0 = m_1\tilde{\lambda} + \mathcal{O}(\tilde{\lambda}^2, r_2\tilde{\lambda}) + (y_{\text{start}} - y_2^\ell) + (y_2^r - y_{\text{end}}), \tag{44}
$$

with $\lambda(w) = r_2(\lambda_2^{\text{mc}} + \tilde{\lambda}(\bar{w}))$. In this sense $\tilde{\lambda}(\bar{w})$ captures the deviation from the maximal canard value which is required to attain the periodic orbit $\gamma(\bar{w};\varepsilon)$. In order to satisfy (44), we see we must have

$$
\tilde{\lambda}(\bar{w}) \sim \underbrace{(y_2^\ell - y_{\text{start}})}_{I_\ell} + \underbrace{(y_{\text{end}} - y_2^r)}_{I_r}, \tag{45}
$$

and we would like to understand the dependence of this expression on $\bar{w}$.

We note that the first term I_ℓ captures the distance from $\mathcal{C}_\varepsilon^{\ell,\text{base}}$, while the second term I_r measures the distance from $\mathcal{C}_\varepsilon^{r,\text{base}}$. Furthermore, the second term, which represents the contraction along $\mathcal{C}_\varepsilon^r$ in backwards time, is monotone in $\bar{w}$. The first term, representing the contraction along $\mathcal{C}_\varepsilon^\ell$ is similarly monotone for small values of $\bar{w}$, but then transitions to oscillatory behavior for values of $\bar{w} > w_0$ due to the accumulated rotation along $\mathcal{C}_\varepsilon^\ell$. Depending on which of these terms is dominant, we either expect to see oscillatory (wiggly) or monotone bifurcation diagrams for the associated canards.

To see this, we note that each branch of the critical manifolds $\mathcal{C}_0^{\ell/r}$ has an associated reduced flow, obtained by implicitly solving for (v, d) as functions of w and plugging into the reduced equation (22), resulting in reduced equations which we denote by

$$
w' = h_\ell(w, \lambda) \tag{46}
$$

along $\mathcal{C}_0^\ell$, and by

$$
w' = h_r(w, \lambda) \tag{47}
$$

along $\mathcal{C}_0^r$. We define for $w > w_{\text{f}}$ the quantities

$$
\begin{aligned}
R_\ell(w) &= \int_{w_{\text{f}}}^{w} \frac{\Re\nu_\ell^+(s)}{h_\ell(s,\lambda)}\mathrm{d}s \\
R_r(w) &= \int_{w_{\text{f}}}^{w} \frac{\nu_r^+(s)}{h_r(s,\lambda)}\mathrm{d}s
\end{aligned} \tag{48}
$$

where ν_ℓ^+, ν_r^+ are as in Hypothesis 1. For the term I_r, the contraction along $\mathcal{C}_\varepsilon^r$ in backwards time occurs approximately at the exponential rate

$$
(y_{\text{end}} - y_2^r) \sim \exp\left(-\frac{R_r(\bar{w})}{\varepsilon}\right) \tag{49}
$$

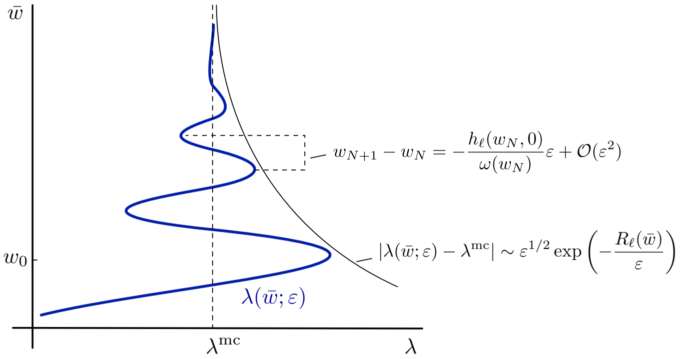

FIGURE 10. Schematic wiggly canard bifurcation diagram of fast jump height $\bar{w}$ versus λ. The fold envelope and distance between successive folds are given by (53) and (61), respectively.

while for I_ℓ, ignoring any rotation, the contraction along $\mathcal{C}^\ell_\varepsilon$ in forwards time is approximately

$$(y^\ell_2 - y_{\mathrm{start}}) \sim \exp\left(-\frac{R_\ell(\bar{w})}{\varepsilon}\right). \tag{50}$$

We make the following assumption.

Hypothesis 5. There exists $w_2 > w_1 \geq w_0$ such that $R_r(\bar{w}) > R_\ell(\bar{w})$ for $\bar{w} \in (w_1, w_2)$, where $R_r(\bar{w}), R_\ell(\bar{w})$ are given by (48).

Remark 6. If the term I_r dominates, that is $R_\ell(\bar{w}) > R_r(\bar{w})$, so that

$$\tilde{\lambda}(\bar{w}) \sim (y_{\mathrm{end}} - y^r_2), \tag{51}$$

then $\tilde{\lambda}(\bar{w})$ is to leading order monotone and exponentially decaying. In particular, we do not expect to see sequences of folds in the associated bifurcation diagram.

Under Hypothesis 5, for values of $\bar{w} \in (w_1, w_2)$, the term I_ℓ dominates, so that

$$\tilde{\lambda}(\bar{w}) \sim (y^\ell_2 - y_{\mathrm{start}}). \tag{52}$$

This separation function oscillates for values of $\bar{w} > w_0$, and we anticipate the appearance of folds as $\tilde{\lambda}(\bar{w})$ snakes back and forth, with an exponentially decaying "fold envelope" (see Figure 10), which decays approximately according to the exponential rate

$$|\lambda(\bar{w};\varepsilon) - \lambda^{\mathrm{mc}}| = |\varepsilon^{1/2}\tilde{\lambda}(\bar{w})| \sim \varepsilon^{1/2}\exp\left(-\frac{R_\ell(\bar{w})}{\varepsilon}\right). \tag{53}$$

To determine the amount of rotation which occurs, we consider in more detail the passage near the slow manifold $\mathcal{C}^\ell_\varepsilon$, and in particular we assume that $\bar{w} > w_0$, since any rotation that occurs must occur in the region $w > w_0$; see Figure 9. We recall from Hypothesis 1 that for $w > w_0$, $\nu^+_\ell(w) = -\alpha(w) + i\omega(w)$, and hence after a linear change of coordinates, at the linear level the flow near $\mathcal{C}^\ell_\varepsilon$ takes the form

$$\begin{aligned} \dot{x}_1 &= -\alpha x_1 + \omega x_2 \\ \dot{x}_2 &= -\omega x_1 - \alpha x_2 \\ \dot{w} &= \varepsilon h_\ell(w, \lambda) \end{aligned} \tag{54}$$

or, in polar coordinates

$$\begin{aligned} \dot{r} &= -\alpha r \\ \dot{\theta} &= \omega \\ \dot{w} &= \varepsilon h_\ell(w, \lambda). \end{aligned} \tag{55}$$

The change in θ over the interval $w \in (w_0, \bar{w})$ is given by

$$|\Delta\theta| \sim \frac{1}{\varepsilon}\left|\int_{w_0}^{\bar{w}} \frac{\omega(s)}{h_\ell(s, \lambda^{\mathrm{mc}})}\mathrm{d}s\right|. \tag{56}$$

We expect a fold, or wiggle, to occur whenever θ crosses $k\pi$ for $k \in \mathbb{N}$, and hence the number of folds N_{wiggle} is asymptotically

$$N_{\mathrm{wiggle}} \sim \frac{1}{\pi\varepsilon}\left|\int_{w_0}^{\bar{w}} \frac{\omega(s)}{h_\ell(s, \lambda^{\mathrm{mc}})}\mathrm{d}s\right|. \tag{57}$$

4.2. **Fold asymptotics for $N \sim \mathcal{O}(1/\varepsilon)$.** Based on the analysis in the previous section, we expect that the Nth fold occurs at the value $w = w_N$ defined implicitly by the relation

$$N = \frac{1}{\pi\varepsilon}\left|\int_{w_0}^{w_N} \frac{\omega(s)}{h_\ell(s, \lambda^{\mathrm{mc}})}\mathrm{d}s\right|, \tag{58}$$

with the λ-value determined via the exponential scaling

$$|\lambda(w_N) - \lambda^{\mathrm{mc}}| \sim \varepsilon^{1/2}\exp\left(-\frac{R_\ell(w_N)}{\varepsilon}\right). \tag{59}$$

It's important here that $N \sim \mathcal{O}(1/\varepsilon)$, in order for the first relation (58) to hold. In particular, this implies that $w_N > w_0 + \Delta w$ for some $\Delta w > 0$ fixed independent of ε, and that the distance between consecutive folds satisfies $w_{N+1} - w_N \sim \mathcal{O}(\varepsilon)$. In fact we can compute this quantity to leading order by solving

$$(N+1) - N = -\frac{1}{\pi\varepsilon}\int_{w_N}^{w_{N+1}} \frac{\omega(s)}{h_\ell(s, \lambda^{\mathrm{mc}})}\mathrm{d}s, \tag{60}$$

from which we obtain

$$w_{N+1} - w_N = -\frac{\pi h_\ell(w_N, 0)}{\omega(w_N)}\varepsilon + \mathcal{O}(\varepsilon^2). \tag{61}$$

To determine the scaling ratio of λ between consecutive folds as $\varepsilon \to 0$, we compute the quantity

$$\begin{aligned} \log\left(\frac{|\lambda(w_{N+1}) - \lambda^{\mathrm{mc}}|}{|\lambda(w_N) - \lambda^{\mathrm{mc}}|}\right) &\sim \frac{R_\ell(w_N) - R_\ell(w_{N+1})}{\varepsilon} \\ &= \frac{1}{\varepsilon}\int_{w_N}^{w_{N+1}} \frac{\alpha(s)}{h_\ell(s, \lambda^{\mathrm{mc}})}\mathrm{d}s \\ &= \frac{(w_{N+1} - w_N)}{\varepsilon}\left(\frac{\alpha(w_N)}{h_\ell(w_N, 0)} + \mathcal{O}(\varepsilon)\right) \\ &= -\frac{\pi\alpha(w_N)}{\omega(w_N)} + \mathcal{O}(\varepsilon) \end{aligned} \tag{62}$$

where we used (61) in the last equality.

4.3. **Fold asymptotics for $N \sim \mathcal{O}(1)$.** If we instead let $\varepsilon \to 0$ for fixed N, all of the oscillations around the slow manifold $\mathcal{C}^\ell_\varepsilon$ occur nearby the critical node-to-focus transition at $w = w_0$. Here the frequency of oscillation around $\mathcal{C}^\ell_\varepsilon$ is small, i.e. not $\mathcal{O}(1)$ in ε, so the distance between wiggles cannot be computed to leading order using the integral of the frequency $\omega(w)$ as in the previous subsection, and we must analyze the more delicate dynamics in a neighborhood of the so-called Airy point.

Near the critical node-to-focus transition in the fast dynamics along the slow manifold $\mathcal{C}^\ell_0$ at $(v, d, w) = (v_0, d_0, w_0)$, without loss of generality the system can be transformed to the system [3, 5]

$$\begin{aligned} \dot{\tilde{v}} &= \tilde{d} + \text{h.o.t.} \\ \dot{\tilde{d}} &= \tilde{w}\tilde{v} + \text{h.o.t.} \\ \dot{\tilde{w}} &= \varepsilon\kappa h_\ell(w_0, 0) + \text{h.o.t.} \end{aligned} \tag{63}$$

where

$$\begin{aligned} e^{\frac{\text{tr}A}{2}t} \begin{pmatrix} \tilde{v} \\ \tilde{d} \end{pmatrix} &= \begin{pmatrix} \frac{1}{a_{12}} & 0 \\ \frac{a_{11}-a_{22}}{2} & 1 \end{pmatrix} \begin{pmatrix} v - v_0 \\ d - d_0 \end{pmatrix} + \text{h.o.t.} \\ \tilde{w} &= \kappa(w - w_0) + \text{h.o.t.} \end{aligned} \tag{64}$$

and

$$\kappa = \frac{\partial}{\partial w}\left(\frac{(\text{tr}A)^2}{4} - \text{det}A\right)\bigg|_{w=w_0} \tag{65}$$

where the matrix A is the linearization of the fast subsystem

$$A = \begin{pmatrix} a_{11} & a_{12} \\ a_{21} & a_{22} \end{pmatrix} = D_{(v,d)}F(v, d, w, 0, 0)\big|_{(v,d)=(v_0,d_0)}. \tag{66}$$

Ignoring higher order terms, and solving for $\tilde{w}$ in terms of t, we obtain the leading order equation for $\tilde{v}$

$$\ddot{\tilde{v}} = \varepsilon\kappa h_\ell(w_0, 0)t\tilde{v} \tag{67}$$

which admits two linearly independent solutions in terms of Airy functions Ai, Bi, which can be re-expressed in terms of the variable $\tilde{w}$ (note $h_\ell < 0$) as

$$\begin{aligned} \tilde{v}_1(\tilde{w}) &= \text{Ai}\left(-\frac{\tilde{w}}{(\varepsilon\kappa h_\ell(w_0, 0))^{2/3}}\right) \\ \tilde{v}_2(\tilde{w}) &= \text{Bi}\left(-\frac{\tilde{w}}{(\varepsilon\kappa h_\ell(w_0, 0))^{2/3}}\right). \end{aligned} \tag{68}$$

Based on the analysis in [5], generically one expects that turning points of λ corresponding to wiggles are related to zeros of the Airy function Ai. In particular, noting (62), the distance between successive wiggles is related to the difference $w_{N+1} - w_N$ between the w-coordinates of the corresponding fast jump traversed by the canard orbit in question. For those orbits whose fast jump occurs near $w = w_0$, that is, near the Airy point, the difference $w_{N+1} - w_N$ should be given in terms of the distance between successive zeros of Ai.

Letting $J_k < 0$ denote the zeros of Ai with $|J_1| < |J_2| < \ldots$. Using the scaled variable in (68), zeros occur whenever

$$\tilde{w} = -\left(\varepsilon\kappa h_\ell(w_0, 0)\right)^{2/3} J_k \tag{69}$$

for some k. Using the fact that $\tilde{w} = \kappa(w - w_0) +$ h.o.t. , we can express the difference

$$w_{N+1} - w_N = \frac{(\varepsilon h_\ell(w_0, 0))^{2/3}}{\kappa^{1/3}}(J_N - J_{N+1}) + \text{h.o.t.} \tag{70}$$

We can see from this expression that the distance between the jump heights of successive folds scales to leading order as $\varepsilon^{2/3}$, in contrast to the $\mathcal{O}(\varepsilon)$-scaling from (61). Proceeding similarly as in §4.2, we substitute (70) into (62) and find that

$$\begin{aligned} \log\left(\frac{|\lambda(w_{N+1}) - \lambda^{\text{mc}}|}{|\lambda(w_N) - \lambda^{\text{mc}}|}\right) &\sim \frac{R_\ell(w_N) - R_\ell(w_{N+1})}{\varepsilon} \\ &= \frac{(w_{N+1} - w_N)}{\varepsilon}\left(\frac{\alpha(w_0)}{h_\ell(w_0, 0)} + \mathcal{O}(\varepsilon)\right) \\ &= -\frac{\alpha(w_0)}{(\varepsilon\kappa h_\ell(w_0, 0))^{1/3}}(J_{N+1} - J_N) + \text{h.o.t.} \end{aligned} \tag{71}$$

5. Numerical examples.

The first numerical example is a synthetic one that is designed to mirror the analysis in the preceding two sections, where the $\mathcal{C}_0^{\ell,r}$ extend to infinity. The second example is the FitzHugh-Nagumo travelling wave system that was our original motivating example. All numerical computations are carried out in Auto [11].

5.1. A synthetic example system.

We consider the following two fast / one slow system inspired by the previous analysis

$$\begin{aligned} \dot{v} &= A(v; \epsilon, \varphi, \delta) + s_\epsilon^-(v; \varphi)d - w \\ \dot{d} &= -d + s_\epsilon^-(v; \varphi)\nu B(v; \varphi, \psi) \\ \dot{w} &= \varepsilon(v + \lambda) \end{aligned} \tag{72}$$

where

$$A(v; \epsilon, \varphi, \delta) = v^2[-s_\epsilon^-(v, \varphi) - s_\epsilon^+(v, \varphi)] - s_\epsilon^-(v; \varphi)[v + \varphi - \varphi^2] + s_\epsilon^+(v; \varphi)[\delta v + \varphi^2 - \delta\varphi],$$

$$B(v; \varphi, \psi) = \frac{v^2}{2} + (1 + \psi)v + \frac{1}{2}(1 + 2\psi)\varphi^2$$

and $s_\epsilon^\pm(v; \varphi)$ are smoothed out versions of cut-off functions that switch for on for $|x| > \varphi$, for a positive parameter φ:

$$s_\epsilon^+(v; \varphi) = \frac{1}{2}\left[1 - \tanh\left(\frac{v + \varphi}{\epsilon}\right)\right], \qquad s_\epsilon^-(v; \varphi) = \frac{1}{2}\left[1 + \tanh\left(\frac{v - \varphi}{\epsilon}\right)\right],$$

for a small parameter $0 < \epsilon \ll 1$. The other parameters ψ, ε, δ, λ and ν are all assumed to be positive. Here ε and λ play the same role as in the analysis. The model is constructed in such a way that it is of the form (25) for small $(d, v, w) = (x, z, y)$ and that the critical manifold is analytic for all $\epsilon > 0$ and is continuous for $\epsilon = 0$. Specifically, for $\epsilon = 0$, then for $x > \varphi$, the left and right-hand portions of the critical manifold are such that w is a linear function of v and of slopes -1 and δ, respectively and the linearisation of the fast flow about them has eigenvalues that are precisely

$$\mathcal{C}^\ell : -1 \pm \sqrt{\nu}\sqrt{(1 + \psi)\varphi + v} \qquad \mathcal{C}^r : -1, \delta.$$

Thus, for $\delta > 1$ we should expect folds on the branch of periodic orbits born at the Hopf bifurcation point, as it approaches the canard cycle, and for $\delta < 1$ we should not expect any. This is precisely what we see.

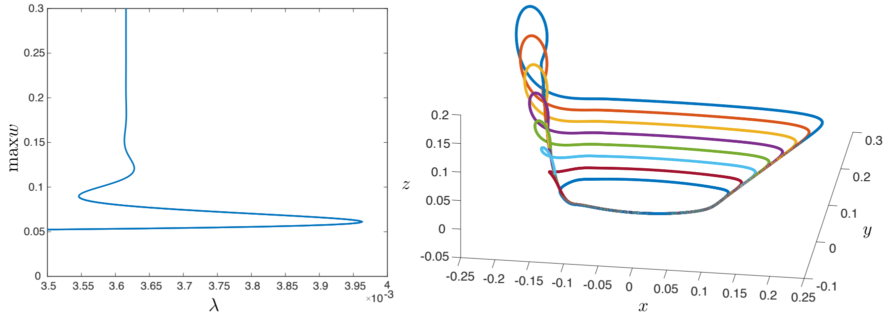

FIGURE 11. (Left) Results of one-parameter continuation in λ of periodic orbits of the synthetic example (72) for $\delta = 2$ and $\varepsilon = 0.1$. (Right) orbits at each of the fold points in the left-hand panel.

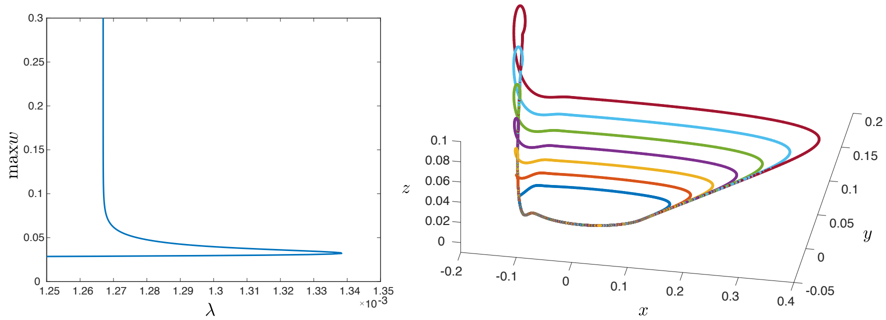

FIGURE 12. Similar to Fig. 12 but for $\delta = 0.5$ and $\varepsilon = 0.02$. The orbits in the right-hand plot are depicted for even increments in period between 60 and 120.

The numerical experiments are carried out for

$$\psi = 0.2, \quad \epsilon = 0.01, \quad \varphi = 0.1, \quad \nu = 50, \tag{73}$$

and $\delta = 2$ or $\delta = 0.5$ with λ and ε as bifurcation parameters.

Note that in the notion of (55) we have for $v < -(1+\psi)\varphi$ that

$$\alpha = 1, \qquad \omega = \nu\sqrt{-v-(1+\psi)\varphi} = \sqrt{-50v-6}, \qquad h_\ell = (v+\lambda),$$

and that Airy point occurs for $v = -(1+\psi)\varphi = -0.12$, for the parameter values chosen.

Now, on $\mathcal{C}^\ell$ we can express $w = -v-\varphi+\varphi^2+\nu B(v;\varphi,\psi)$, which can be inverted to give

$$v = -(\psi+1)\varphi - \frac{\sqrt{1+\psi^2\varphi^2\nu^2+(2w-2\varphi(1+\psi))\nu}}{\nu} = -\frac{1}{10} - \frac{\sqrt{100w-1}}{50}$$

for the parameter values (73).

Therefore we have

$$\omega(w) = \sqrt{-1+\sqrt{100w-1}}, \quad \text{and} \quad \frac{h_\ell(w,\lambda)}{\omega(w)} = \frac{50\lambda-\sqrt{100w-1}-5}{50\sqrt{-1+\sqrt{100w-1}}} \tag{74}$$

N	$w_{N+1}-w_N$	$-\varepsilon\pi h_\ell/\omega$	abs. error	$\log\left(\frac{\lvert\lambda(w_{N+1})-\lambda^{\mathrm{mc}}\rvert}{\lvert\lambda(w_N)-\lambda^{\mathrm{mc}}\rvert}\right)$	$\pi/\alpha/\omega$
2	0.007800	0.009120	0.297041	-3.134495	-3.312145
3	0.007810	0.008331	0.143856	-2.766146	-2.914168
4	0.007659	0.007844	0.088228	-0.752243	-2.656183

TABLE 1. Computation versus asymptotic prediction for $w_{N+1} - w_N$ and for the accummulation rate of λ-values for the explicitly constructed model with $\delta = 2$ and $\varepsilon = 0.02$. Here the second column gives the computed values of the difference between successive w_N-values and the third column gives the value that this ratio should have according to (61), where h_ℓ is estimated using (74). The fourth column gives the absolute error between these two quantities. The fifth column gives the computed value of the left-hand-side of the expression (62) that determines the rate of accummulation of λ-values for the case that $N = \mathcal{O}(1/\varepsilon)$. The final column of the table gives the value of the right-hand-side of (62) for the given value of w_N.

N	$w_{N+1}-w_N$	$-\varepsilon\pi h_\ell/\omega$	abs. error	$\log\left(\frac{\lvert\lambda(w_{N+1})-\lambda^{\mathrm{mc}}\rvert}{\lvert\lambda(w_N)-\lambda^{\mathrm{mc}}\rvert}\right)$	$\pi/\alpha/\omega$
2	0.010474	0.013585	0.229015	-2.670591	-3.312145
3	0.010851	0.012412	0.125764	-2.500844	-2.914168
4	0.010742	0.011690	0.081075	-1.963004	-2.656183
5	0.010570	0.011208	0.056862	-2.607696	-2.474712
6	0.010398	0.010861	0.042625	0.821494	-2.338275

TABLE 2. Similar to Table 1 but for $\varepsilon = 0.03$, in which case additional fold curves could be computed.

Using these values we have used Auto to compute curves of folds along the path of periodic orbits emanating from the Hopf bifurcation. The results are plotted in Figs. 11–13. Specifically, Fig. 11 is consistent with the theory that there should be a finite number of folds along the periodic orbit branch for $\delta > 1$, whose λ-values converge to that of the canard cycle as the amplitude of the cycle grows in amplitude. In contrast, Fig. 12, which is for $\delta < 1$, suggests an eventually monotonic convergence in parameter to the canard value.

Figure 13 shows the result of continuing the first seven folds depicted in Fig. 11 in ε and λ. The left-hand end of each branch for small ε is where that fold can no longer be reliably computed owing to it being exponentially close to λ^{mc}. Note that the chosen values of ε are not particularly small, $\mathcal{O}(10^{-2})$, but there is a compromise in the numerical computations between choosing an ε-value that is small enough for the theory to apply, but large enough that sufficiently many folds can be accurately computed. Note from the three zooms of the curves in the (ε, λ)-plane just how rapid this convergence is, even for these moderate ε-values.

For each of $\varepsilon = 0.02$ and 0.03 we use the maximum value of w along the orbit at the Nth fold as a proxy for w_N and compute the theoretical limit in the case $N \sim \mathcal{O}(1/\varepsilon)$ (61) for $w_{N+1} - w_N$ for small ε using the computed value of λ and $(w_N + w_{N+1})/2$ in (74). The results are shown in the first four columns of Tables 1

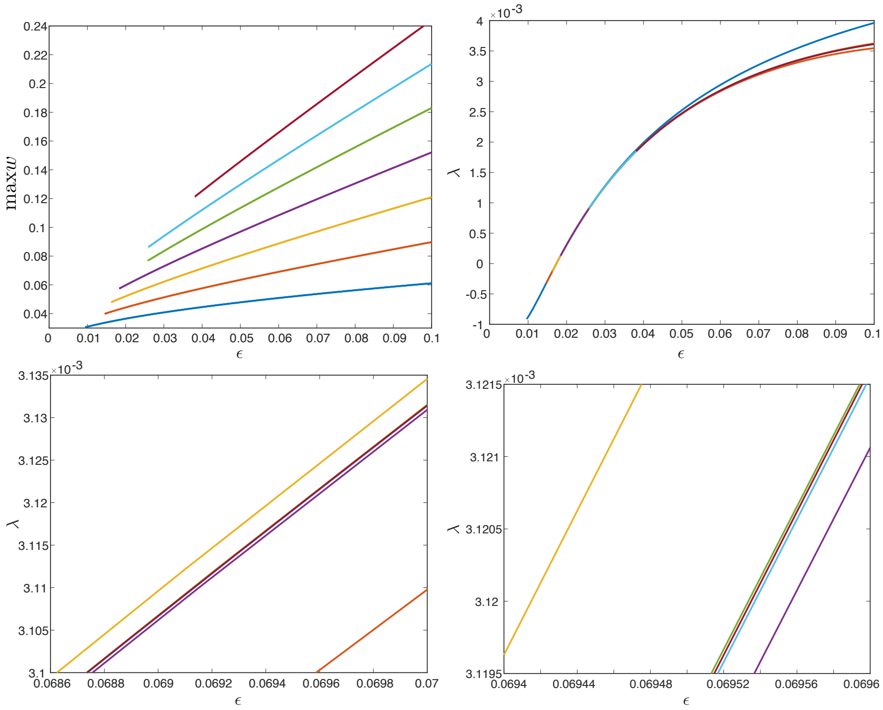

FIGURE 13. (Top) 2-parameter continuation of folds of solutions in Fig. 11. (Bottom) two successive zooms of the data in the top right plot

and 2 for $\varepsilon = 0.02$ and 0.03, respectively. In both cases we see that there is a good agreement with the theoretical result, even for these moderate values of ε and N. We note too that the agreement gets better, which can be seen in the reduction of the absolute error as N increases.

Next we consider numerical evidence for the exponential convergence of the λ-values of the folds according to (62) under the assumption that $N = \mathcal{O}(1/\varepsilon)$. Here we compute an estimate for λ^{mc} by computing the vertical asymptote of the numerically computed branch of periodic orbits. Note from the final two columns of Tables 1 and 2 that the computed logarithm is close to that predicted in theory, except for the largest N for which we have computed a fold. This final discrepancy appears to be due to the difference between the fold and the maximal canard parameter values being close to the order of the numerical precision.

Finally, we deal with the distinction between the two asymptotic estimates in ε, (61) and (70), for the values w_N in the two cases $N \sim \mathcal{O}(1)$ and $N \sim \mathcal{O}(1/\varepsilon)$, respectively. Figure 14 shows the computed difference between successive w-values of

$$\Delta_N = w_{N+1} - w_N$$

as a function of ε for the first few computed folds along the wiggly canard.

While the evidence is far from definitive, as one would expect for the moderate values of ε we were reliably able to compute folds for, Figure 14 provides persuasive numerical evidence that the asymptotic estimates (61) and (70) are obeyed for this

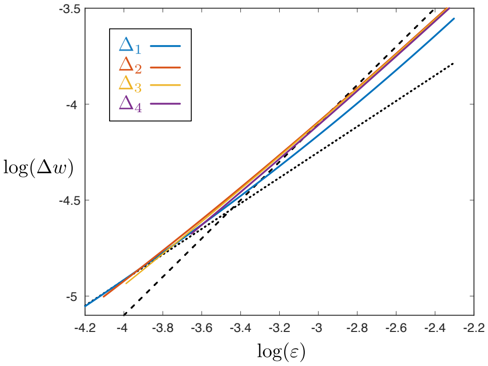

FIGURE 14. Computed differences in w-values of successive folds as a function of ε, plot on a log-log scale. Also plotted for reference are straight lines with slopes 1 (dashed line) and 2/3 (dotted lines).

example. In particular the theory would predict that the first 'few' values of Δ_N — say, for $N < N_0$ for some $N_0 > 0$ — should scale like $\varepsilon^{2/3}$ as $\varepsilon \to 0$, with the remaining ones scaling like ε. Moreover the number N_0 increases approximately linearly with ε. Thus, each curve of Δ_N versus ε should have slope that approaches 1 on a log-log scale for large ε and approaches 2/3 on a log-log scale as $\varepsilon \to 0$. Moreover, the transition between the two scaling laws should occur for lower ε with each higher N. A comparison with lines of slopes 1 and 2/3 in the figure, strongly suggest that such a transition between the two asymptotic estimates indeed occurs in this example.

5.2. **The FitzHugh–Nagumo equations.** We now return to the FitzHugh–Nagumo equations (3). Based on the discussion in §2, it is not difficult to see that for $\lambda = p = 0$, and $0 < s < \frac{2D}{\sqrt{3}}$, the system (3) satisfies Hypotheses 1–4 under the reversal $\xi \to -\xi$; see, for instance [4] for details on the structure of the fast layer problem (4) and the canard dynamics near the equilibrium $(v, d, w) = (0, 0, 0)$. Here $\mathcal{C}_0^1$ and $\mathcal{C}_0^2$ play the roles of the manifolds $\mathcal{C}_0^r$ and $\mathcal{C}_0^\ell$, respectively (note that the left/right orientation of $\mathcal{C}_0^1$ and $\mathcal{C}_0^2$ in Figure 3 is flipped compared to that of $\mathcal{C}_0^r$ and $\mathcal{C}_0^\ell$ in Figure 4).

As described in §2, and by the theory in §3, the local canard explosion in (3) originates at a singular Hopf bifurcation, after which the canard orbits grow to $\mathcal{O}(1)$ size, and then continue to grow in an exponentially thin interval in the parameter λ. The upper part of the bifurcation branch (corresponding to the canard cycles "with head") exhibits several folds, and the six uppermost folds are labelled in the upper left panel of Figure 15. There is in fact one additional fold "higher up" visible along the canard explosion branch; however this fold appears in the regime of relaxation oscillations and does not arise from the same mechanism which produces each of the others, so we ignore it for the purposes of the current discussion.

The number of such folds associated with canards-with-head grows in ε, but folds cannot be reliably continued along the lower part of the branch, in the region of canards-without-head. We offer an explanation for this discrepancy, based on the theory in §4. In particular, we show that Hypothesis 5 is satisfied along the portion of the branch corresponding to canards-with-head, but not for the canards-without-head.

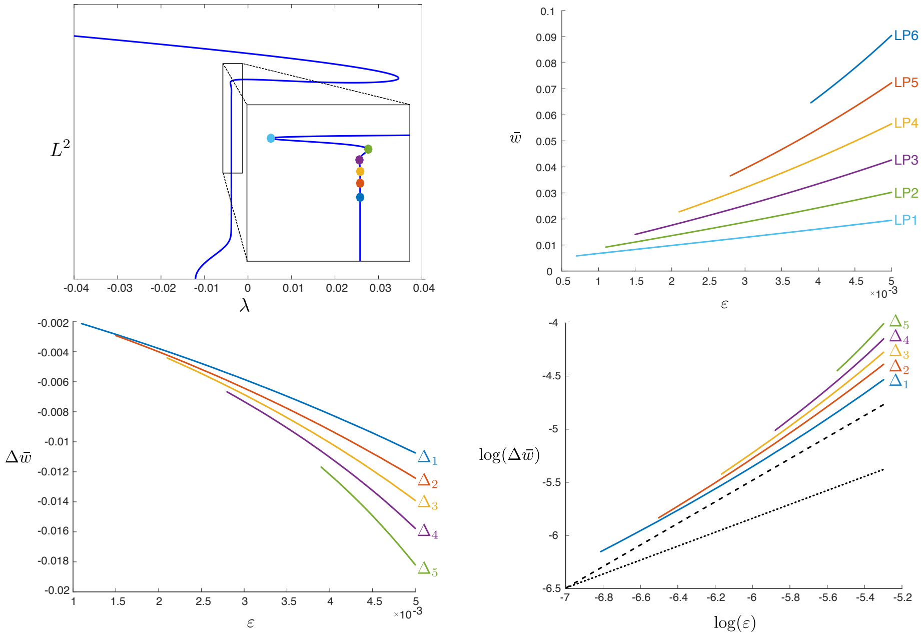

FIGURE 15. Results of continuation of folds in the FitzHugh–Nagumo system (3) for $\gamma = 0, s = 0.65$. Top left: Plot of L^2-norm versus the parameter λ for the canard explosion of traveling wavetrains in (3) for $\varepsilon = 0.005$. Shown in the inset is a zoom of the location of the first (highest) six folds. Top right: Plotted is the jump height $\bar{w}$ of the first six folds for decreasing ϵ. Bottom panels: Plotted are the differences between the jump heights of successive folds for decreasing ε as a standard plot (left) and log-log plot (right).

To see this, we briefly describe the difference in geometry of each of these orbits. The canards without head, are formed by traversing the left branch $\mathcal{C}_0^1$ of the critical manifold, followed by the middle branch $\mathcal{C}_0^2$, then traversing a fast jump back to $\mathcal{C}_0^1$ to complete a closed orbit, much like the geometry of the general system in Sec. 3.2. However, the canards-with-head have a different geometry, in that the orbit first traverses the left branch $\mathcal{C}_0^1$, followed by the middle branch $\mathcal{C}_0^2$, then a fast jump to the rightmost branch $\mathcal{C}_0^3$, and finally a second jump back to $\mathcal{C}_0^1$ near the upper right fold point.

In each case, one could anticipate the appearance of snaking canards with an increasing number of folds as $\varepsilon \to 0$, as both the canards with head and those without each traverse an orbit segment connecting $\mathcal{C}_0^1$ to the middle branch branch $\mathcal{C}_0^2$, a portion of which satisfies Hypothesis 1. In particular, based on the discussion in §2, we have that any canard orbit which passes near the portion of $\mathcal{C}_0^2$ lying between $v_- < v < v_+$ will experience rotation due to the focus structure of the layer equation, and the corresponding canard explosion branch may exhibit snaking. It is clear that this is the case for the canards with or without head, provided that the jump height $\bar{w}$ from the middle branch (to either $\mathcal{C}_0^1$ or $\mathcal{C}_0^3$), satisfies $f(v_-;0) < \bar{w} < f(v_+;0)$.

In this setting, we expect snaking behavior to occur provided Hypothesis 5 is satisfied. However, this hypothesis has a different meaning for the canards with versus without head. For those without head, this hypothesis can be checked directly as in §4, i.e. we need to compare the relative contraction rates along the manifolds $\mathcal{C}_0^1$ and $\mathcal{C}_0^2$ between $w = 0$ and the jump height $w = \bar{w}$.

To compute the relevant quantities $R_r(\bar{w})$ and $R_\ell(\bar{w})$, we recall the reduced equations for the FitzHugh–Nagumo system (6), given by

$$w' = \frac{1}{s}(v - \gamma w) \tag{75}$$

where $f(v; \lambda) = w$ on the slow manifold. For values of w in between the two fold points, there are three solutions of the equation $f(v; \lambda) = w$, given by $v_i(w), i = 1, 2, 3$ corresponding to the three branches $\mathcal{C}_0^i, i = 1, 2, 3$ of the critical manifold $\mathcal{C}_0$. In the limit $\varepsilon \to 0$, we can evaluate $R_r(\bar{w})$ and $R_\ell(\bar{w})$ more naturally parameterizing the slow flow by the v coordinate, whence we obtain

$$v' = \frac{(v - \gamma f(v; 0))}{s f'(v; 0)}. \tag{76}$$

We note that in the case of FitzHugh–Nagumo system, the middle branch is repelling, so we must compare the expansion along $\mathcal{C}_0^2$, expressed by the real part of the eigenvalue $\nu^+(v)$ given in (8), with the contraction along $\mathcal{C}_0^1$, expressed by the eigenvalue $\nu^-(v)$ given in (8). We can then express the quantities $R_r(\bar{w})$ and $R_\ell(\bar{w})$ as

$$R_\ell(\bar{w}) = \int_0^{v_2(\bar{w})} \frac{s f'(v; 0) \Re \nu^+(v)}{(v - \gamma f(v; 0))} \mathrm{d}v, \qquad R_r(\bar{w}) = \int_0^{v_1(\bar{w})} \frac{s f'(v; 0) \nu^-(v)}{(v - \gamma f(v; 0))} \mathrm{d}v \tag{77}$$

Figure 16 depicts the difference $R_\ell(\bar{w}) - R_r(\bar{w})$ (blue curve) as a function of $\bar{w}$. It is apparent that this quantity is briefly positive, then becomes negative at approximately $\bar{w} \approx 0.039$, so that Hypothesis 5 is satisfied for values of $\bar{w} > 0.039$.

However, in the case of canards with head, while the contraction along $\mathcal{C}_0^2$ is computed similarly as in the previous case, the portion of the orbit spent near $\mathcal{C}_0^1$ is longer, and the relevant contraction rate must be computed between $w = 0$ and $w = w_*$, where w_* is the height of the second jump, back to $\mathcal{C}_0^1$ near the upper fold point. This means that the contraction along $\mathcal{C}_0^1$ is "amplified" compared with the previous case, and we must replace $R_r(\bar{w})$ with $R_r(w_*)$. In the limit $\varepsilon \to 0$, the height w_* of this second jump can be found by searching for a heteroclinic orbit ϕ_{31} the layer problem 4 for the parameter values $D = 1, p = \lambda = 0$, and $s = 0.65$ which connects the right branch $\mathcal{C}_0^3$ of the critical manifold to the left branch $\mathcal{C}_0^1$. A computation shows that this occurs when

$$w_* := f\left(\frac{1}{3} + \frac{\sqrt{2}}{3} s; 0\right) \approx 0.147 \tag{78}$$

Figure 16 depicts the difference $R_\ell(w_*) - R_r(\bar{w})$ (red curve) as a function of $\bar{w}$, which is clearly negative on the entire interval, so that Hypothesis 5 is satisfied for all $\bar{w} < w_*$. Furthermore, using the condition (12), we compute that for $D = 1, \lambda = 0, s = 0.65$, the Airy point at which the fast dynamics in the layer problem switches from node to focus along the middle branch $\mathcal{C}_0^2$ occurs for $w \approx 0.0031$, so that oscillations (and corresponding snaking) can occur for any orbits with jump height $\bar{w} > 0.0031$.

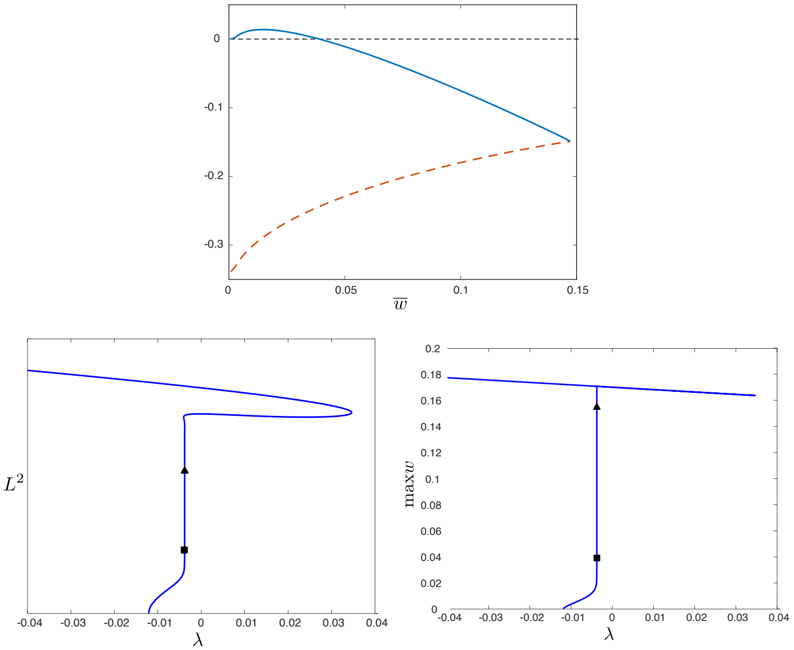

FIGURE 16. (Top) Shown is the way-in-way-out function given by the difference $R_\ell(w_*) - R_r(\bar{w})$ (dashed red) plotted versus $\bar{w}$ for the case of canards with head, as well as the difference $R_\ell(\bar{w}) - R_r(\bar{w})$ (solid blue) in the case of canards without head. In the latter case, the quantity $R_\ell(\bar{w}) - R_r(\bar{w})$ is briefly positive between $\bar{w} = 0$ and $\bar{w} \approx 0.039$. The bottom left and right panels, respectively, depict plots of the L^2 norm versus λ and the maximum height w along the orbit versus λ for the canard explosion of wave trains in (3) for $\gamma = 0, s = 0.65, \varepsilon = 0.005$. The square denotes the location along the bifurcation branch where the way-in-way-out quantity $R_\ell(\bar{w}) - R_r(\bar{w})$ switches from positive to negative; hence one does not expect to observe folds below this location. The triangle denotes the approximate transition point above which the orbits correspond to canards with head and below which correspond to canards without head.

The effect of this discrepancy in the way-in-way-out computation for the canards with versus without head is that for the canards without head, the potential snaking region only begins for orbits at a jump height $\bar{w} > 0.039$. These orbits experience a much larger exponential contraction (in reverse time) along the branch $\mathcal{C}_0^2$ and thus any oscillations (and the corresponding fold envelope (53)) which occur along this branch will be exponentially "squeezed" compared to those in the case of the canards with head, which occur for orbits with jump height of only $\bar{w} > 0.0031$. Figure 17 depicts the convergence of the jump heights as $\varepsilon \to 0$ for the canards with head, which approach the Airy point at $\bar{w} \approx 0.0031$.

In summary, based on the formal computations in §4, for the parameter values $s = 0.65, \gamma = 0, D = 1$ and sufficiently small $\varepsilon > 0$, we predict the appearance of snaking along the canard explosion in (3), although any snaking along the portion of

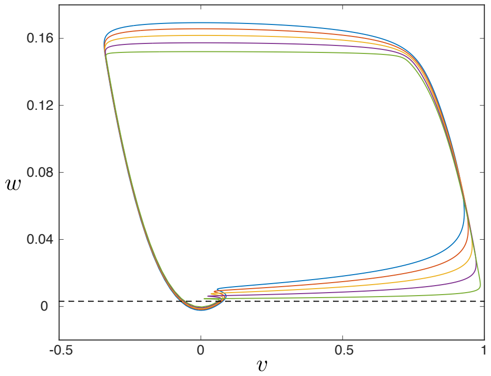

FIGURE 17. Shown are orbits in (v, w)-space along the continuation of the fold LP1 for values of $\varepsilon = \{0.005, 0.004, 0.003, 0.002, 0.001\}$ (blue, red, yellow, purple, green). The dashed black line denotes the location of the Airy transition at $w \approx 0.0031$.

the branch corresponding to canards without head will be exponentially suppressed (and thus much more difficult to detect numerically) than the snaking which occurs along the portion containing canards with head.

This explains why the upper left panel of Figure 15 depicts visible snaking along the upper portion of the branch, but not along the lower portion. Figure 15 also shows the results of continuing the six highest folds in AUTO for decreasing ε. Due to the exponentially small variance in the location of the folds as $\varepsilon \to 0$, AUTO becomes unreliable for small ε, particularly for folds of higher index (hence the different ending points of each branch). Also depicted are the jump heights $\bar{w}$ of the canard orbits associated with each fold, as well as the differences between successive jump heights of neighboring folds, plotted in both a standard and log-log plot. We can see convergence of the latter plot towards what appears to be a common curve, though it was difficult to resolve the folds numerically for any smaller values of ε. Also plotted are lines of slope 1 (dashed) and 2/3 (dotted); we observe that for smaller values of ε, the slope of the Δ_1 curve dips noticeably below 1, as the jump height approaches the critical height of the Airy point along $\mathcal{C}_0^2$, where the results of §4.3 imply that the difference between the jump heights of successive folds increases from $\mathcal{O}(\varepsilon)$ to $\mathcal{O}(\varepsilon^{2/3})$.

6. Conclusion.

This paper has provided a generic analysis of canard growth in singularly perturbed systems of ODEs with two fast variables and one slow when the linearization around one portion of the slow manifold is of focus type. We show that under a sign condition on the relative closeness to the imaginary axis of the eigenvalues governing the flow close to the attracting and repelling parts of the slow manifold, that the canard growth of a limit cycle is accompanied by a sequence of fold bifurcations. The overall effect is to see a wiggly bifurcation curve of periodic orbits, which is reminiscent of that close to a Shilnikov homoclinic orbit under an analogous sign condition. Here though, it is the amplitude rather than the period of the periodic orbit that grows as the bifurcation curve traverses a sequence of folds. In the present context though, for each finite value of the singular parameter ε, there are at most finitely many folds. Nevertheless the asymptotic scaling of the folds as the number of folds become large is remarkably similar to that close to a Shilnikov homoclinic orbit (cf. (1) and (62)).

Our numerical explorations in §5.2 confirmed this qualitative behavior in the FitzHugh–Nagumo system (3), demonstrating the appearance of this family of folds, and also providing an explanation for the observation that the folds are more pronounced along the portion of the canard explosion corresponding to the canards "with head".

While sharing a resemblance to the wiggly bifurcation curve which occurs near a Shilnikov homoclinic orbit, the geometry of the present situation is rather distinct. In the Shilnikov case, the folds which occur along the bifurcation branch are associated with the local oscillatory behavior near a saddle-focus equilibrium as the period grows and the periodic orbits approach the homoclinic limit. In the present study, rather than the local saddle-focus structure of an equilibrium, it is the focus structure in the layer problem along a slow manifold which forms the basis for the sequence of folds in the bifurcation branch. That is, it is the Airy transition point along the slow manifold which accounts for the oscillations and hence the folds in the bifurcation branch.

While these two phenomena are not directly related in (2) (the Airy point is not near the equilibrium of the full system (3)), there are nevertheless connections. We recall from Remark 1 that the wiggly canard explosion phenomenon studied here is reminiscent of that which is found along a pulse-replicating branch of traveling *pulse* solutions in (2), in which a single pulse transforms into a double pulse along a canard transition [5] in a nearby parameter regime $(\lambda, s) \sim (0, 1/\sqrt{2})$ and $p = 0$. This pulse-replicating branch exhibits a similar (and closely related) sequence of folds, growing in number as $\varepsilon \to 0$. The single pulse is itself a Shilnikov homoclinic orbit to the equilibrium $(v, d, w) = (0, 0, 0)$ which is of saddle-focus type in the relevant parameter regime. There are therefore two mechanisms at play, the oscillatory behavior in the pulse tails due to the saddle-focus equilibrium, and the oscillatory behavior around the middle branch of the slow manifold due to the presence of the Airy point, the latter of which is responsible for the folds in the bifurcation branch as the pulse transitions into a double pulse. It is also this latter effect that manifests in the wiggly bifurcation branch analyzed in the present study.

With these traveling pulses in mind, we briefly comment on the stability of the traveling wave trains as solutions of the PDE (2). The sequence of folds which occur along the pulse-replicating branch have implications for the stability of the associated traveling pulse solutions; the folds are linked to the accumulation of eigenvalues on the so-called "slow absolute spectrum" of the traveling pulses [3]. We expect that the folds (or lack of folds) depending on the relevant way-in-way-out computation encountered here have similar implications for structure of the spectra of the associated wave trains, but this is beyond the scope of the present work. We expect that this problem is quite challenging, as even the spectral stability of the large, relaxation oscillation wave trains (such as the green orbit in Figure 2), which we expect are stable, is nontrivial. These and related stability questions for traveling canard orbits in (2) are the subject of ongoing work.

We believe our results go a long way to explaining previous results that showed a seemingly wiggly canard-like growth in a number of systems, starting with the second author's PhD thesis, which considered a fluid-forced double pendulum system, see [7]. They also provide explanation for how a sequence of folds accompany the canard-like growth exhibited along a branch of traveling pulses in (2), as studied

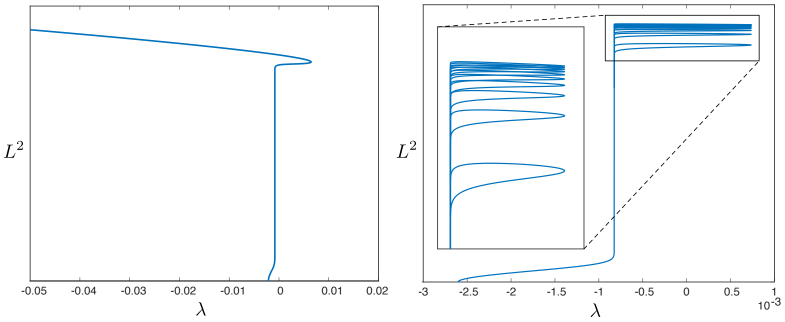

FIGURE 18. Canard explosion in the FitzHugh–Nagumo equation (3) for $\varepsilon = 0.001$ in the case $s = 0.72$ (left) and $s = 0.65$ (right). In the latter case, the canard explosion does not result in a family of relaxation oscillations, but rather a continuous spike-adding sequence through which additional large amplitude oscillations are accumulated via repeated canard explosions. The inset shows a zoom of this family of canard explosions along the upper portion of the branch.

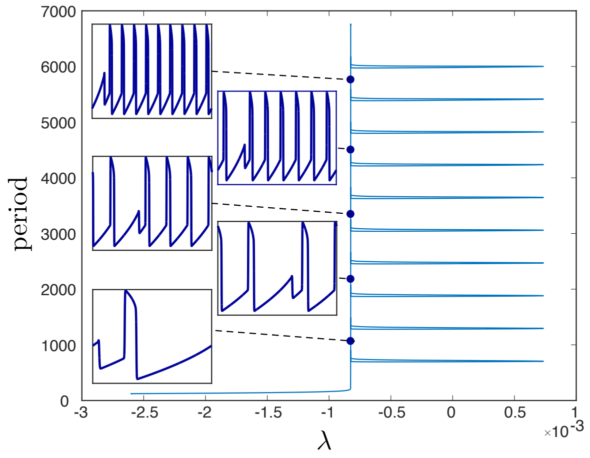

FIGURE 19. Shown is a plot of period versus λ for the canard explosion in the case $\varepsilon = 0.001, s = 0.65$ as in Figure 18. The v-profiles for periodic wave trains with $1, 3, 5, 7$, and 9 spikes, respectively, are depicted in the insets at various points along the spike adding branch. Each such profile is plotted over one period, which increases when moving vertically along the branch as additional spikes are added.

in the PhD thesis of the first author, some 20 years later, see [5]. In both these models, there is also numerical evidence that the same wiggly canard process accounts for the mechanism by which mixed-mode periodic waves grow additional large-amplitude pulses.

To point to possible future work that extends the results here to explaining such spike-adding, we briefly present further numerical continuation results of the branch of wave-trains in the FitzHugh-Nagumo system, beyond the initial canard explosion. By shrinking ε slightly to $\varepsilon = 0.001$, we find that the behavior of this branch depends critically on the value of the wave speed s; see Figure 18 which depicts the canard explosion branch for $\varepsilon = 0.001$ for values of $s = 0.72$ and $s = 0.65$. In the former case, the canards grow into a family of relaxation oscillations which continues indefinitely, while in the latter case, the branch folds back and undergoes successive canard explosions, each of which adds an additional large-amplitude spike to the wave train pattern. Figure 19 depicts the profiles of the resulting wave trains.

To understand this discrepancy, we return to the layer problem (4). It can be shown [5, 6] that for $\lambda = 0$ the front ϕ_{31} only exists for values of $s < 1/\sqrt{2}$ for a critical height $w_* = w_*(s)$ (and a similar statement holds for ϕ_{13}). On the other hand, for values of $s \geq 1/\sqrt{2}$, the fronts ϕ_{21} and ϕ_{23} exist for all values of w between the two fold points, and critical fronts ϕ_{f3} and ϕ_{f1} exist which connect the lower left fold (resp. upper right fold) to the branch $\mathcal{C}_0^3$ (resp. $\mathcal{C}_0^1$).

Provided $\varepsilon > 0$ is taken sufficiently small, the result of this difference in the geometry of the associated wave trains is that for values of $s \geq 1/\sqrt{2}$, the canard explosion grows into the family of relaxation oscillations formed by orbits which traverse $\mathcal{C}_0^1$ and $\mathcal{C}_0^3$, jumping between these branches precisely at the fold points. However for values of s slightly below $1/\sqrt{2}$, because the fast jumps ϕ_{31} and ϕ_{13} do not exist precisely at the fold points, the resulting gap allows the branch to fold back on itself and undergo an additional canard explosion, growing a secondary large amplitude excursion. This process appears to repeat indefinitely; this in contrast to the pulse replication behavior also observed in (3), in which a 1-pulse can grow into an 2-pulse, a 2-pulse into a 3-pulse, and so on, but adjacent pulse replication branches are disconnected [3]. This behavior is also distinct from typical spike-adding behavior analyzed in bursting models [10, 29, 31, 37], in that in the present case the entire initial large-amplitude oscillation is replicated during each spike-adding event.

A precise explanation of this connection between wiggly canards, spike adding and the morphology of mixed-mode travelling waves is left for future work, as is the development of a rigorous justification of the formal asymptotic estimates that form the core of this paper.

Acknowledgments. The authors thank Mathieu Desroches for helping inspire this project and for extensive discussions during its early stages. The first author acknowledges support through NSF grant DMS-2016216.

REFERENCES

[1] E. Benoît, J.-L. Callot, F. Diener and M. Diener, Chasse au canard, *Collect. Math.*, **32** (1981), 37–119.

[2] P. Carter, Spike-adding canard explosion in a class of square-wave bursters, *J. Nonlinear Sci.*, **30** (2020), 2613–2669.

[3] P. Carter, J. D. M. Rademacher and B. Sandstede, Pulse replication and accumulation of eigenvalues, *SIAM J. Math. Anal.*, **53** (2021), 3520–3576.

[4] P. Carter and B. Sandstede, Fast pulses with oscillatory tails in the FitzHugh–Nagumo system, *SIAM J. Math. Anal.*, **47** (2015), 3393–3441.

[5] P. Carter and B. Sandstede, Unpeeling a homoclinic banana in the FitzHugh–Nagumo system, *SIAM J. Appl. Dyn. Syst.*, **17** (2018), 236–349.

[6] P. Carter and A. Scheel, Wave train selection by invasion fronts in the FitzHugh–Nagumo equation, *Nonlinearity*, **31** (2018), 5536–5572.

[7] A. R. Champneys, Homoclinic orbits in the dynamics of articulated pipes conveying fluid, *Nonlinearity*, **4** (1991), 747–774.

[8] A. R. Champneys, V. Kirk, E. Knobloch, B. E. Oldeman and J. Sneyd, When shil'nikov meets hopf in excitable systems, *SIAM J. Appl. Dyn. Syst.*, **6** (2007), 663–693.

[9] M. Desroches, J. Guckenheimer, B. Krauskopf, C. Kuehn, H. M. Osinga and M. Wechselberger, Mixed-mode oscillations with multiple time scales, *SIAM Rev.*, **54** (2012), 211–288.

[10] M. Desroches, T. J. Kaper and M. Krupa, Mixed-mode bursting oscillations: Dynamics created by a slow passage through spike-adding canard explosion in a square-wave burster, *Chaos: An Interdisciplinary Journal of Nonlinear Science*, **23** (2013), 046106, 13 pp.

[11] E. Doedel, B. Oldeman *et al.*, Auto-07p: Continuation and bifurcation software for ordinary differential equations, 2020, Latest version at `https://github.com/auto-07p`.

[12] F. Dumortier and R. Roussarie, Canard cycles and center manifolds, *Mem. Amer. Math. Soc.*, **121** (1996), no. 577, 100 pp.

[13] C. Fall, E. Marland, J. Wagner and J. Tyson, *Computational Cell Biology*, Springer-Verlag, New York, 2002.

[14] R. FitzHugh, Impulses and physiological states in theoretical models of nerve membrane, *Biophysical journal*, **1** (1961), 445–466.

[15] P. Gaspard, R. Kapral and G. Nicolis, Bifurcation phenomena near homoclinic systems; A two-parameter analysis, *J. Stat. Phys.*, **35** (1984), 697–727.

[16] P. Glendinning and C. Sparrow, Local and global behaviour near homoclinic orbits, *J. Stat. Phys.*, **35** (1984), 645–696.

[17] J. Guckenheimer and C. Kuehn, Homoclinic orbits of the FitzHugh–Nagumo equation: The singular-limit, *Discrete Contin. Dyn. Syst. Ser. S*, **2** (2009), 851–872.

[18] J. Guckenheimer and C. Kuehn, Homoclinic orbits of the FitzHugh–Nagumo equation: Bifurcations in the full system, *SIAM J. Appl. Dyn. Syst.*, **9** (2010), 138–153.

[19] S. P. Hastings, On the existence of homoclinic and periodic orbits for the FitzHugh-Nagumo equations, *Quart. J. Math. Oxford Ser.*, **27** (1976), 123–134.

[20] S. P. Hastings, Single and multiple pulse waves for the FitzHugh–Nagumo equations, *SIAM J. Appl. Math.*, **42** (1982), 247–260.

[21] C. Jones, N. Kopell and R. Langer, Construction of the FitzHugh-Nagumo pulse using differential forms, in *Patterns and Dynamics in Reactive Media*, Springer, 1991, 101–115.

[22] T. Kaper and C. Jones, A primer on the exchange lemma for fast-slow systems, vol. 122 of *The IMA Volumes in Mathematics and its Applications*, 65–87, Springer, New York, 2001.

[23] J. Keener and J. Sneyd, *Mathematical Physiology*, 2nd edition, Springer-Verlag, New York, 2009.

[24] M. Krupa, B. Sandstede and P. Szmolyan, Fast and slow waves in the FitzHugh–Nagumo equation, *J. Differential Equations*, **133** (1997), 49–97.

[25] M. Krupa and P. Szmolyan, Extending geometric singular perturbation theory to nonhyperbolic points—fold and canard points in two dimensions, *SIAM J. Math. Anal.*, **33** (2001), 286–314.

[26] M. Krupa and P. Szmolyan, Relaxation oscillation and canard explosion, *J. Differential Equations*, **174** (2001), 312–368.

[27] C. Kuehn, *Multiple Time Series Dynamical Systems*, Springer-Verlag, Heidelberg, 2015, Applied Mathematical Sciences, vol. 191.

[28] Y. Kuznetsov and A. Panfilov, Stochastic waves in the FitzHugh-Nagumo system, 1981, Research Computing Centre, USSR Academy of Sciences, Pushchino. In Russian.

[29] D. Linaro, A. Champneys, M. Desroches and M. Storace, Codimension-two homoclinic bifurcations underlying spike adding in the Hindmarsh–Rose burster, *SIAM J. Appl. Dyn. Syst.*, **11** (2012), 939–962.

[30] J. Nagumo, S. Arimoto and S. Yoshizawa, An active pulse transmission line simulating nerve axon, *Proceedings of the IRE*, **50** (1962), 2061–2070.

[31] H. Osinga and K. Tsaneva-Atanasova, Dynamics of plateau bursting depending on the location of its equilibrium, *Journal of Neuroendocrinology*, **22** (2010), 1301–1314.

[32] J. D. M. Rademacher, *Homoclinic Bifurcation from Heteroclinic Cycles with Periodic Orbits and Tracefiring of Pulses*, Ph.D. thesis, University of Minnesota, 2004, http://www.math.uni-bremen.de/~jdmr/pub/dissMay7Web.pdf.

[33] L. Shilnikov, On the generation of a periodic motion from trajectories doubly asymptotic to an equilibrium state of saddle type, *Math. USSR Sb.*, **6** (1968), 427–438.

[34] L. Shilnikov, A. Shilnikov, D. Turaev and L. Chua, *Method of Qualitative Theory of Nonlinear Dynamics: Part II*, World Scientific, Singapore, 2001.

[35] C. Soto-Trevino, *Geometric Methods for Periodic Orbits in Singularly Perturbed Systems*, Ph.D. Thesis, Boston University, 1998.

[36] P. Szmolyan and M. Wechselberger, Canards in $\mathbb{R}^3$, *J. Differential Equations*, **177** (2001), 419–453.

[37] D. Terman, Chaotic spikes arising from a model of bursting in excitable membranes, *SIAM J. Appl. Math.*, **51** (1991), 1418–1450.

[38] M. Wechselberger, Existence and bifurcation of canards in $\mathbb{R}^3$ in the case of a folded node, *SIAM J. Appl. Dyn. Syst.*, **4** (2005), 101–139.

Received August 2021; revised January 2022; early access February 2022.

E-mail address: `pacarter@uci.edu`
E-mail address: `a.r.champneys@bristol.ac.uk`